

1           **Ground-based observations of Saturn’s auroral**  
2           **ionosphere over three days: trends in  $H_3^+$  temperature,**  
3           **density and emission with Saturn local time and**  
4           **planetary period oscillation**

5           James O’Donoghue<sup>d,a</sup>, Henrik Melin<sup>a</sup>, Tom S. Stallard<sup>a</sup>, G. Provan<sup>a</sup>,  
6           Luke Moore<sup>d</sup>, Sarah V. Badman<sup>e</sup>, Stan W.H. Cowley<sup>a</sup>, Kevin H. Baines<sup>c</sup>,  
7           Steve Miller<sup>b</sup>, and James S.D. Blake<sup>a</sup>

8           <sup>a</sup>*Department of Physics and Astronomy, University of Leicester, Leicester, LE1 7RH, UK*

9           <sup>b</sup>*Atmospheric Physics Laboratory, Department of Physics and Astronomy, University College*  
10           *London, London, WC1E 6BT, UK*

11           <sup>c</sup>*NASA Jet Propulsion Laboratory, M/S 183-601, 4800 Oak Grove Drive, Pasadena, CA 91109,*  
12           *USA*

13           <sup>d</sup>*Center for Space Physics, Boston University, Boston, MA 02215, USA*

14           <sup>e</sup>*Department of Physics, Lancaster University, UK*

15   *Key words:* Saturn, aurora, magnetosphere, ionosphere, atmosphere

---

## Abstract

On 19 to 21 April 2013, the ground-based 10-metre W.M. Keck II telescope was used to simultaneously measure  $H_3^+$  emissions from four regions of Saturn's auroral ionosphere: 1) the northern noon region of the main auroral oval; 2) the northern midnight main oval; 3) the northern polar cap and 4) the southern noon main oval. The  $H_3^+$  emission from these regions was captured in the form of high resolution spectral images as the planet rotated. The results herein contain twenty-three  $H_3^+$  temperatures, column densities and total emissions located in the aforementioned regions - ninety-two data points in total, spread over timescales of both hours and days. Thermospheric temperatures in the spring-time northern main oval are found to be cooler than their autumn-time southern counterparts by tens of K, consistent with the hypothesis that the total thermospheric heating rate is inversely proportional to magnetic field strength. The main oval  $H_3^+$  density and emission is lower at northern midnight than it is at noon, in agreement with a nearby peak in the electron influx in the post-dawn sector and a minimum flux at midnight. Finally, when arranging the northern main oval  $H_3^+$  parameters as a function of the oscillation period seen in Saturn's magnetic field - the planetary period oscillation (PPO) phase - we see a large peak in  $H_3^+$  density and emission at  $\sim 115^\circ$  northern phase, with a full-width at half-maximum (FWHM) of  $\sim 44^\circ$ . This seems to indicate that the influx of electrons associated with the PPO phase at  $90^\circ$  is responsible at least in part for the behavior of all  $H_3^+$  parameters. A combination of the  $H_3^+$  production and loss timescales and the  $\pm 10^\circ$  uncertainty in the location of a given PPO phase are likely, at least in part, to be responsible for the observed peaks in  $H_3^+$  density and emission occurring at a later time than the peak precipitation expected at  $90^\circ$  PPO phase.

# 38 1 Introduction

## 39 1.1 Ionosphere

40 Saturn's ionosphere is thought to be dominated by the positive ions  $\text{H}^+$  and  $\text{H}_3^+$  between 900  
41 - 3000 km altitude and by hydrocarbon ions (e.g.  $\text{C}_3\text{H}_5^+$ ) between 500 - 900 km altitude, along  
42 with their companion electrons, which maintain the ionosphere's quasi-neutrality (*Moses and*  
43 *Bass*, 2000). Co-located with this is the thermosphere, the charge-neutral component of the  
44 upper atmosphere, which is composed chiefly of H and  $\text{H}_2$ . Charged particles in the ionosphere  
45 are continuously generated by ionising the otherwise neutral thermosphere through two main  
46 mechanisms. The first, photo-ionisation by solar extreme ultra-violet (EUV) radiation, acts  
47 across the entire sunlit portion of the planet (the dayside). The second, electron impact ioni-  
48 sation, acts primarily in the polar regions of the planet. Both mechanisms also electronically,  
49 vibrationally and rotationally excite the atmospheric constituents, which in turn de-excite  
50 and emit photons. The emissions from these mechanisms are 'auroral' emissions and occur at  
51 multiple wavelengths including infrared (IR), visible and ultraviolet (UV). This paper focuses  
52 primarily on the infrared emissions emanating from the molecular ion  $\text{H}_3^+$  near the poles of the  
53 planet.

54 Saturn's ionosphere lies at the base of the planetary magnetosphere, a region formed by  
55 the confinement of the planetary magnetic field by the solar wind. Closed field lines extend  
56 in the equatorial region to distances  $\sim 22 R_S$  ( $R_S$  is Saturn's 1 bar equatorial radius, equal  
57 to 60,268 km) on the dayside (*Radioti et al.*, 2013), while open field lines stretch into a long  
58 magnetic tail downstream from the planet on the nightside. From estimates of the open flux  
59 in the magnetotail, the boundary between open and closed field lines in the ionosphere typi-  
60 cally lies at around planetocentric co-latitude  $\sim 15^\circ$  in each hemisphere (*Badman et al.*, 2006),  
61 the difference between the two reflecting the north-south quadrupole asymmetry of Saturn's  
62 planetary magnetic field (*Burton et al.*, 2010). In general it is expected that field-aligned cur-

63 rents flow down into the ionosphere over the polar field region due to the sub-corotation of  
 64 plasma on open field lines and in the outer magnetosphere (*Bunce et al.*, 2008). The current  
 65 then flows from the pole towards the equator in both hemispheres as ionospheric Pedersen  
 66 currents, before returning up the field lines to the magnetosphere at lower latitudes as the  
 67 flow returns to near-rigid corotation with the planet (e.g. *Cowley and Bunce*, 2003; *Cowley*  
 68 *et al.*, 2004). The main auroral oval emissions are related to the latter ring of upward current  
 69 (downward electron precipitation). The auroral oval is thus expected to lie in the region just  
 70 equatorward of the open-closed boundary where the plasma angular velocity rises from low  
 71 values on open lines towards rigid corotation on closed lines. The main oval is in general taken  
 72 to correspond to the region between co-latitudes of  $\sim 10^\circ$  and  $\sim 20^\circ$  in both hemispheres (see,  
 73 e.g., *Carbary*, 2012, and references therein). Auroral emissions are also sometimes observed  
 74 in the poleward region, likely associated with solar wind-magnetosphere coupling dynamics  
 75 at the magnetopause boundary of the magnetosphere (e.g. *Meredith et al.*, 2014). Here we  
 76 present new observations of  $\text{H}_3^+$  obtained with the Keck telescope in April 2013 using similar  
 77 methodology to that employed by *O'Donoghue et al.* (2014). These observations measure the  
 78 northern and southern main auroral ovals simultaneously as in the previous study, but this  
 79 time they take place over three days instead of one, allowing for a wider ranging analysis  
 80 of short term auroral behavior. In addition, due to the developing northern spring season at  
 81 Saturn, the dataset presented here also includes and discusses simultaneous measurements of  
 82 both the northern polar aurora as well as the midnight main auroral oval, owing to the viewing  
 83 geometry at the time of the observations.

## 84 1.2 The $\text{H}_3^+$ probe at Saturn

85 The molecular ion  $\text{H}_3^+$  is produced by the reaction  $\text{H}_2 + \text{H}_2^+ \longrightarrow \text{H}_3^+ + \text{H}$  (*Oka*, 2006). The  
 86 reaction time (the ion chemistry timescale) varies from 10 seconds at 800 km altitude to 1000

87 seconds for altitudes near 2000 km (*Badman et al.*, 2014). The lifetime of  $\text{H}_3^+$  is proportional  
88 to its temperature, inversely proportional to the ionospheric electron density and has been  
89 previously quoted as 500 seconds (*Melin et al.*, 2011). During this lifetime,  $\text{H}_3^+$  becomes ther-  
90 mally excited to a higher rotational-vibrational (ro-vibrational) state by neighboring molecules  
91 on timescales of  $10^{-2}$  s, which is approximately the same time for the ion to relax to a lower  
92 state and emit a photon. The discrete emission line spectra of  $\text{H}_3^+$  make it a useful probe of  
93 the conditions in Saturn's ionosphere for two reasons. The first is that  $\text{H}_3^+$  parameters such as  
94 column-integrated temperature, density and power output (hereafter, total emission) can be  
95 derived from it (e.g. *Miller et al.*, 2006; *Melin et al.*, 2014). Secondly, it is considered to be in  
96 local thermodynamic equilibrium (LTE) - or at least quasi-LTE - with its surroundings (*Miller*  
97 *et al.*, 1990; *Moore et al.*, 2008), meaning that the ion temperature is equivalent to the neutral  
98 temperature.

99 Using the ground-based 3.8-metre United Kingdom InfraRed Telescope (UKIRT), the south-  
100 ern auroral  $\text{H}_3^+$  temperature was found to be  $380 \pm 70$  K in 1999 and  $420 \pm 70$  K in 2004 by *Melin*  
101 *et al.* (2007). Later, in 2007, the Visual and Infrared Mapping Spectrometer (VIMS) (*Brown*  
102 *et al.*, 2004) on board Cassini was used to derive a southern polar auroral  $\text{H}_3^+$  temperature of  
103 (on average)  $590 \pm 30$  K over a period of 10 hours (*Stallard et al.*, 2012a). Measurements of the  
104 southern auroral oval at equinox in 2009, also obtained by Cassini VIMS, yielded average tem-  
105 peratures of  $\sim 410$  K (*Lamy et al.*, 2013). The first conjugate northern and southern main oval  
106  $\text{H}_3^+$  temperatures were measured at high spatial resolution in 2011 using the 10-metre W.M.  
107 Keck II (hereafter, Keck) telescope by *O'Donoghue et al.* (2014). The 10 spectral images, when  
108 co-added, yielded an average main auroral  $\text{H}_3^+$  temperature of  $583 \pm 13$  K (south) and  $527 \pm 18$   
109 K (north) over a  $\sim 2$  hour period. Throughout this time interval the spectra gave temperatures  
110 that varied by tens of Kelvins; this was a similar variability to the uncertainties, so it may  
111 be considered real or due to noise. In the neutral thermosphere near the exobase ( $\sim 1900$  km  
112 altitude above the 1 bar surface), solar occultations were performed using the Cassini ultra-

113 violet imaging spectrometer (UVIS) to derive temperatures (*Koskinen et al.*, 2013), yielding  
114 temperatures of 370 K to 540 K from low- to high(auroral)-latitudes, respectively. The inter-  
115 hemispheric temperature asymmetry measured by *O'Donoghue et al.* (2014) was postulated to  
116 be the result of an inversely proportional relationship between magnetic field strength and the  
117 total heating rate. Due to the lower magnetic field strength in the south, the area undergoing  
118 heating is larger in the south than in the north (see *O'Donoghue et al.*, 2014, for a more detailed  
119 discussion). Whilst the thermospheric temperatures at high latitudes can mostly be explained  
120 via auroral region Joule heating (*Cowley et al.*, 2004), the low-latitude high temperatures re-  
121 main difficult to explain theoretically. For example, exospheric temperatures are modeled to  
122 be 143 Kelvin on the basis of solar EUV heating alone, yet observations show the exosphere  
123 to be  $\sim 400$  K (at sub-auroral latitudes) (*Yelle and Miller*, 2004; *Koskinen et al.*, 2013). *Smith*  
124 *et al.* (2007) and *Mueller-Wodarg et al.* (2012) have explored the idea that heat is meridionally  
125 transported down from the poles to the equator, but conclude that auroral heating actually  
126 provides a net cooling effect at low latitudes. This is caused by a circulation pattern in which  
127 high altitude heating (by ion drag) causes equatorward flows. The flow is balanced by the  
128 continuity equation at low altitudes in the form of poleward flows, which themselves require  
129 there be an upwelling of material from below. It is this upwelling material that expands and  
130 cools adiabatically, leading to the counter intuitive effect of low latitude cooling, despite there  
131 being a nearby heating source (*Smith et al.*, 2007). Thus, at present, it appears some addi-  
132 tional source of energy is required to explain equatorial temperatures. One suggestion is the  
133 breaking of gravity waves in the thermosphere, but this is modeled to account for temperature  
134 enhancements of (at most)  $\sim 10$ 's of K (*Barrow and Matcheva*, 2013). A final source of note is  
135 the low-latitude precipitation along the magnetic field lines conjugate to the rings known as  
136 'ring rain'; it is possible that this is also associated with a low-latitude current system between  
137 the rings and the planet, but as yet such currents have not been directly observed (*O'Donoghue*  
138 *et al.*, 2013).

140 In 1980 both Voyager 1 and 2 spacecraft measured bursts of nonthermal radio emission which  
 141 emanated from Saturn - specifically they are likely from the northern hemisphere: the period  
 142 of these bursts were  $\sim 10.67$  hours and taken (provisionally) to be the intrinsic rotation period  
 143 of the planet (*Kaiser et al.*, 1980). However, more recently, during Saturn's pre-equinoctial  
 144 southern summer between 2004 - 2008, the Cassini spacecraft has measured Saturn kilometric  
 145 radiation (SKR) from both the northern and southern hemispheres, finding them to exhibit  
 146 different periods:  $\sim 10.6$  hours in the north and  $\sim 10.8$  hours in the south (although these rates  
 147 are still changing over time) (*Gurnett et al.*, 2009). These emissions, together with magnetic  
 148 field perturbations observed within the magnetosphere, are inferred to be associated with  
 149 two independent current systems rotating in the northern and southern hemispheres with  
 150 slightly differing periods that vary slowly with Saturn's seasons (see, e.g. *Andrews et al.*,  
 151 2008, 2010; *Southwood*, 2011; *Provan et al.*, 2009, 2012, and references therein). Following the  
 152 recent discussion by *Southwood and Cowley* (2014), the empirically-determined current system  
 153 associated with the northern ionosphere, of primary interest here, is shown in Figure 1, in  
 154 a view looking down on the northern pole (a similar current system also flows in the south)  
 155 (*Hunt et al.*, 2014). In this diagram the solid lines and symbols show the currents, while the  
 156 dotted lines represent the associated magnetic field perturbations above the Pedersen layer of  
 157 the ionosphere required by Ampère's law. The primary current system consists of field-aligned  
 158 currents that flow down into the ionosphere on the right of the diagram (circled crosses on the  
 159 inner dashed line ring), across the polar ionosphere as Pedersen currents directed from right  
 160 to left, and out of the ionosphere as field-aligned currents on the left of the diagram (circled  
 161 dots on the black dashed line ring). Secondary field-aligned currents of lesser magnitude and  
 162 opposite polarity also flow on the outer ring, which serve to limit the field perturbations to  
 163 the interior region. This current system then rotates with the northern period,  $\sim 10.64$  h at

164 the time of our observations (compared with  $\sim 10.69$  h for the southern SKR period). Position  
 165 with respect to the rotating pattern is defined by the northern PPO phase function  $\Psi_N$ , which  
 166 increases clockwise around the diagram in Figure 1. Enhanced upward currents, associated  
 167 with enhanced electron precipitation and auroral emissions, are expected to occur for  $\Psi_N \approx$   
 168  $90^\circ$  (modulo  $360^\circ$ ), while enhanced downward currents, likely associated with suppression of  
 169 precipitation and emissions, are expected for  $\Psi_N \approx 270^\circ$ .

170 Empirically, the orientation of the system at any time is determined through examination of  
 171 the related magnetic field oscillations. In particular, if we consider the magnetic perturbations  
 172 between the two current rings (dotted lines in Figure 1), mapped along quasi-dipolar field lines  
 173 into the equatorial magnetosphere, it will be seen that these transform into a quasi-uniform  
 174 field in which the perturbation field points radially outward from the planet at  $\Psi_N \approx 0^\circ$ , radially  
 175 inward at  $\Psi_N \approx 180^\circ$ , and has positive and negative azimuthal components (with respect to  
 176 the northern spin/magnetic pole) at  $\Psi_N \approx 90^\circ$  and  $270^\circ$ , respectively. Magnetic oscillations  
 177 observed in the equatorial magnetosphere are then analysed to determine the azimuth with  
 178 respect to noon at which the northern quasi-uniform perturbation field points radially outward  
 179 at any instant of time,  $\Phi_N(t)$ , thus also defining the azimuth where the northern PPO phase  
 180  $\Psi_N$  takes the value zero (modulo  $360^\circ$ ) at that time. The northern PPO phase as a function  
 181 of azimuth and time is thus given by

$$182 \quad \Psi_N(\phi, t) = \Phi_N(t) - \phi, \tag{1}$$

183 where  $\phi$  is the azimuth in degrees with respect to noon of any observation point (equiva-  
 184 lent to local time), and  $\Phi_N(t)$  is determined empirically, with rotation period given by  $\tau_N$   
 185  $= 360^\circ / (d\Phi_N/dt)$  and with  $\Phi_N$  expressed in degrees. The function  $\Phi_N(t)$  employed here is  
 186 that determined from Cassini magnetic field data by *Provan et al.* (2014). Signatures of this  
 187 planetary period oscillation from the auroral region were first noted from the Voyager 1 and  
 188 2 spacecraft's UV photometer data by *Sandel and Broadfoot* [1981] and *Sandel et al.* [1982].



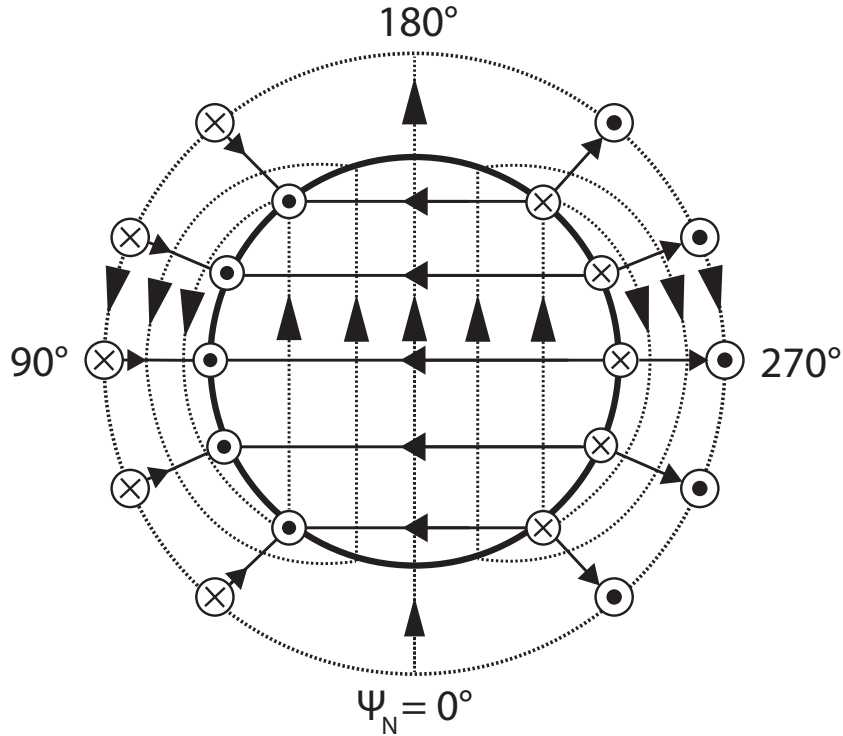


Fig. 1. Sketch of the form of the currents (solid lines and symbols) and perturbation magnetic fields (dotted lines) associated with the northern system PPOs, in a view looking down on Saturn’s northern ionosphere from above. The principal field-aligned currents flow across the inner ring: into the ionosphere on the right (circled crosses), and out of the ionosphere on the left (circled dots), joined by ionospheric Pedersen currents flowing from right to left across the polar ionosphere. Secondary field-aligned currents of smaller magnitude and opposite polarity flow on the outer boundary of the current system, confining the perturbation field to the interior region. The current system rotates anti-clockwise with the northern PPO period  $\tau_N$ . Azimuth with respect to the current system is defined by the phase function  $\Psi_N(\phi, t)$  as shown in the figure (equation (1)), increasing clockwise around the diagram.

189 Using Cassini VIMS, *Badman et al.* [2012a] discovered that the  $H_3^+$  auroral intensity follows a  
 190 sinusoidal function with PPO phase, with  $H_3^+$  peak intensity occurring in the north between  
 191  $\Psi_N \approx 0 - 45^\circ$ , before the expected maximum peak intensity associated with enhanced electron  
 192 precipitation at  $\Psi_N \approx 90^\circ$ .

## 2 Observations

The observations presented here used the 10-m Keck telescope situated on Mauna Kea, Hawaii. They were designed to be an integral part of the Saturn Auroral Observing Campaign of 2013 (this *Icarus* special issue), such that they overlap observations performed by the Cassini spacecraft, Hubble Space Telescope, and the NASA Infrared Telescope Facility (IRTF). The observations took place on the 19, 20, and 21 April and are summarized in Table 1. In this table the quoted times are the actual observing time on Earth (i.e. not corrected for light-travel time from Saturn to Earth) and the ‘seeing’ column refers to blurring of the received light by the Earth’s atmosphere. The quoted central meridian longitudes (CMLs) are from the Saturn system III longitude system [*Kaiser et al.* 1980]. Emissions from these CMLs are light travel time corrected, i.e. the  $\sim 73$  minutes time delay has been accounted for in the results here. During these dates, Saturn was at opposition with respect to the Earth-Sun line with its northern hemisphere tilted towards the Earth and the Sun with both a sub-Earth and sub-solar latitude (coincidentally) of  $18.3^\circ$ , i.e. in conditions of Saturn’s northern spring (summer solstice occurs in 2017). In the previous work, Saturn had a sub-Earth latitude of  $8.2^\circ$  [*O’Donoghue et al.* 2014].

Date	Start UT	End UT	Saturn integration*	CML range	Seeing
19 April	10:55:00	13:11:50	40 min (8)*	43 - 120°	0.4''
20 April	12:18:42	13:18:39	20 min (4)*	181 - 215°	0.45''
21 April	10:40:05	13:24:41	55 min (11)*	217 - 309°	0.6''

Table 1

Summary of Keck telescope observations in April 2013. \*Total time spent observing Saturn itself; the number in parentheses is the number of 5-minute co-additions used.

The instrument used on the Keck telescope was the near infrared spectrometer (NIRSPEC) [*McLean et al.* 1998], which has a spectral resolving power of  $R = \lambda/\Delta\lambda \sim 25,000$  and thus

211 provides a minimum resolution of (e.g.)  $\Delta\lambda \approx 1.59 \times 10^{-4} \mu\text{m}$  at  $3.975 \mu\text{m}$ . The wavelength  
 212 range used here is between  $3.95$  and  $4.0 \mu\text{m}$ , which covers the Q-Branch ( $\Delta J=0$ ) ro-vibrational  
 213 transition lines of  $\text{H}_3^+$ . Saturn's axis of rotation is measured to be co-aligned with the magnetic  
 214 axis to within  $\sim 0.1^\circ$  uncertainty [*Burton et al.* 2010]. Taking advantage of this symmetry, the  
 215 spectrometer slit was orientated in a north-south direction on Saturn as shown in Figure 2.  
 216 The planet is then allowed to rotate beneath the slit whilst spectral images are taken along  
 217 the noon-midnight meridian plane. The slit measures  $0.432''$  width by  $24''$  length with a pixel  
 218 on the CCD corresponding to  $0.144''$  squared on the sky, as in Figure 2.

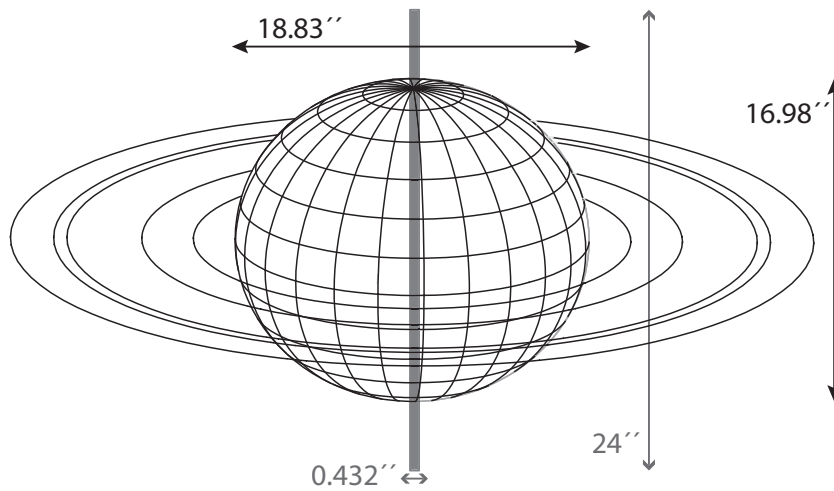


Fig. 2. **Saturn as observed with Keck, April 21 2013.** Saturn's sub-Earth latitude was  $18.3^\circ$  during the observations. The arrowed lines show the angular extent of Saturn and the dimensions of the NIRSPEC spectral slit in seconds of arc.

219 Owing to this viewing geometry we are afforded the ability to collect data from four distinct  
 220 latitudinal ranges:

- 221 (1) Northern midnight main oval (NMMO):  $8 - 15^\circ$  co-latitude (Nightside)
- 222 (2) Northern polar cap (NPC):  $0 - 6^\circ$  co-latitude (Day - Nightside)
- 223 (3) Northern main oval (NMO):  $8 - 22^\circ$  co-latitude (Dayside)
- 224 (4) Southern main oval (SMO):  $18 - 22^\circ$  co-latitude (Dayside)

225 where dayside and nightside correspond to regions sunward and anti-sunward of the krono-  
226 graphic north pole, respectively. These regions of interest are shown in Figure 3 and note that  
227 they all remain lit by the Sun. They were selected (as close as the viewing geometry allowed) to  
228 coincide with the approximate statistical locations of the northern and southern main auroral  
229 ovals between  $\sim 10 - 25^\circ$ , and the polar cap between  $\pm 10^\circ$  of the north pole [*Badman et al.*  
230 2006; *Carbary* 2012]. These regions are associated with internal and external forcing on the  
231 Saturnian magnetosphere, respectively, as discussed in the introduction. An example of the  
232 viewing geometry limitation is at the NPC - here, the spatial resolution of one pixel on the  
233 detector corresponds to  $\sim 3^\circ$  latitude. In addition, and applicable to the whole spectral image,  
234 atmospheric seeing will smear the signal received across multiple pixels. Although the amount  
235 of pixels smeared is constant within the image, the range of latitudes represented by a given  
236 pixel diminishes with increasing latitude. This cross-contamination by light from neighbouring  
237 pixels is taken into account by creating a small separation of between  $\sim 0.144 - 0.288$  seconds  
238 of arc (1 - 2 pixels) between the different regions listed above.

239 Each individual spectral image consists of twelve 5-s integrations, creating exposures 60 s  
240 long, which are of both Saturn ‘A’ and sky ‘B’ frames, with the telescope slewing between each  
241 in the sky in an ABBA pattern. Standard astronomical reduction techniques are employed  
242 to clean the observed spectral images, which include an A-minus-B subtraction in which the  
243 Earth’s sky emissions are removed from the Saturn spectra, and a star flux calibration. The flux  
244 calibration measures the spectrum of a black body emitting star (A0) in order to account for  
245 the wavelength dependent absorption of light by the Earth’s atmosphere, whilst also converting  
246 the CCD photon count into physical photon flux. The star used in this work was HR 5717.  
247 Other reduction procedures include a dark current subtraction and dividing by a ‘flat field’.  
248 Together, these account for thermal emissions at the detector and defects on the CCD chip and  
249 optics, respectively. The reduced spectral images are then co-added into groups of five spectra  
250 (see Table 1) in order to create a single higher signal to noise (S/N) ratio image. However,

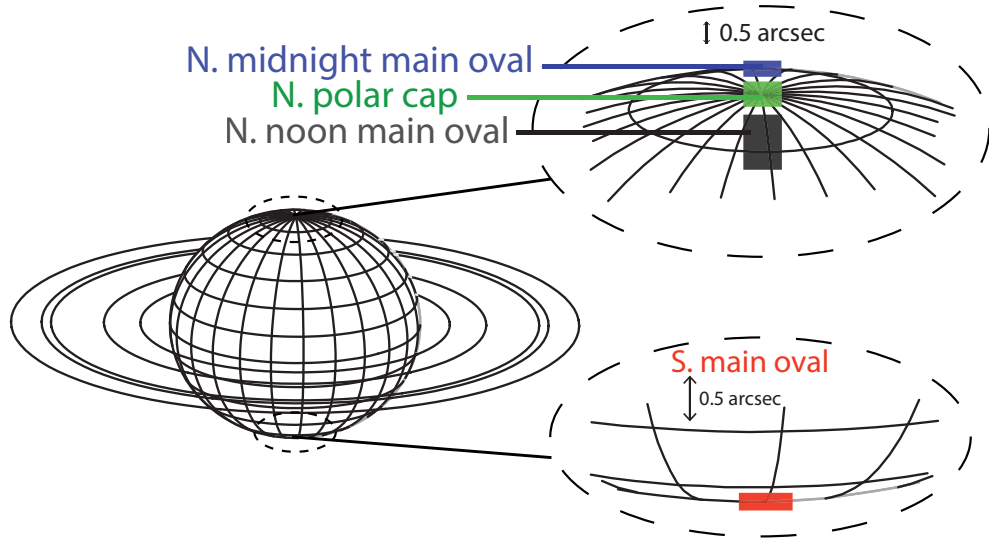


Fig. 3. **Regions of interest on Saturn.** Four distinct color-coded areas are illustrated, corresponding to the regions listed in the text. The chosen color scheme will be used in subsequent figures for clarity. Note that the different colored blocks (not to exact scale) are separated slightly in the north, to avoid cross-contamination introduced by the effects of telluric seeing. Longitude and latitude grid lines represent 15 degree spacings.

251 these spectra are obtained at different times typically within a  $\sim 15 - 20$  minute range; this  
 252 is chiefly because the A frames are often separated by B frames, but more general observing  
 253 time overheads cause this time window to vary, e.g. the telescope slewing time between the A  
 254 and B frame positions, losses in tracking or human error. Within these time ranges we thus  
 255 typically obtain a swath of data spanning  $8 - 11^\circ$  in longitude as the planet rotates beneath  
 256 the slit. In this work we assume an optically thin atmosphere in and above the ionosphere;  
 257 this assumption was used and tested by *Lam et al.* [1997] to be valid.

258 An example of a reduced spectral image (x-axis wavelength, y-axis spatial dimension) which  
 259 has been co-added from all 5-minute integrations on April 21 is shown in Figure 4. In this figure  
 260 there are three main sources of radiation highlighted: the reflection of sunlight from the lower  
 261 atmosphere, the continuum reflection of sunlight from the rings, and discrete  $H_3^+$  emission  
 262 lines. The ability to measure  $H_3^+$  emissions is aided by the fact that hydrocarbons also absorb

263 sunlight at different wavelengths; these are the dark regions on the body of the planet between  
 5 and 19 arcseconds in Figure 4.

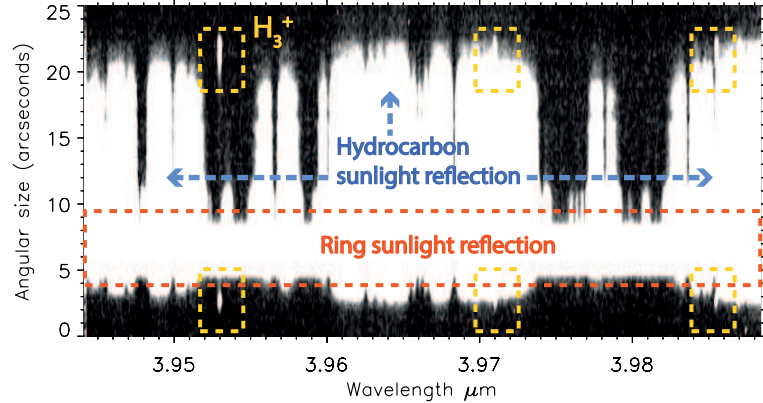


Fig. 4. **An image of the spectrum of Saturn taken at local Saturn noon.** This is the co-addition of all eleven 5-minute integrations on 21 April 2013. The wavelength range is shown on the horizontal axis and the angular size in the sky is shown on the vertical axis. North is at the top of the image and south is at the bottom. Discrete  $H_3^+$  emission line spectra are inside the yellow dashed boxes in the form of white vertical lines (white being high light intensity, black being low/none). From left to right these lines are the  $Q(1,0^-)$ ,  $Q(2,1)$  and  $Q(3,0)$  lines described in the main text. Hydrocarbons such as methane absorb solar radiation (creating the black background) between the auroral regions. The white bar of emission centered at  $\sim 6''$  is the continuum reflection of sunlight from the rings. The remaining white pixels are due to sunlight reflected by hydrocarbons and other molecules.

264

### 265 3 Data analysis

266 For a given temperature, a discrete  $H_3^+$  emission line will emit at a given intensity. We  
 267 produce a theoretical spectrum of multiple lines from a line list of  $H_3^+$  emission for thousands  
 268 of different temperatures [see e.g. *Neale et al.* 1996; *Melin et al.* 2014]. The relative intensities of  
 269 multiple discrete  $H_3^+$  emission lines (i.e. a set of line ratios) represent the effective temperature  
 270 of  $H_3^+$  in quasi-LTE. An example of an observed spectral profile is shown in Figure 5 by the  
 271 black crosses. Three Q-branch ( $\Delta J = 0$ ) intensity peaks are visible from left to right in this

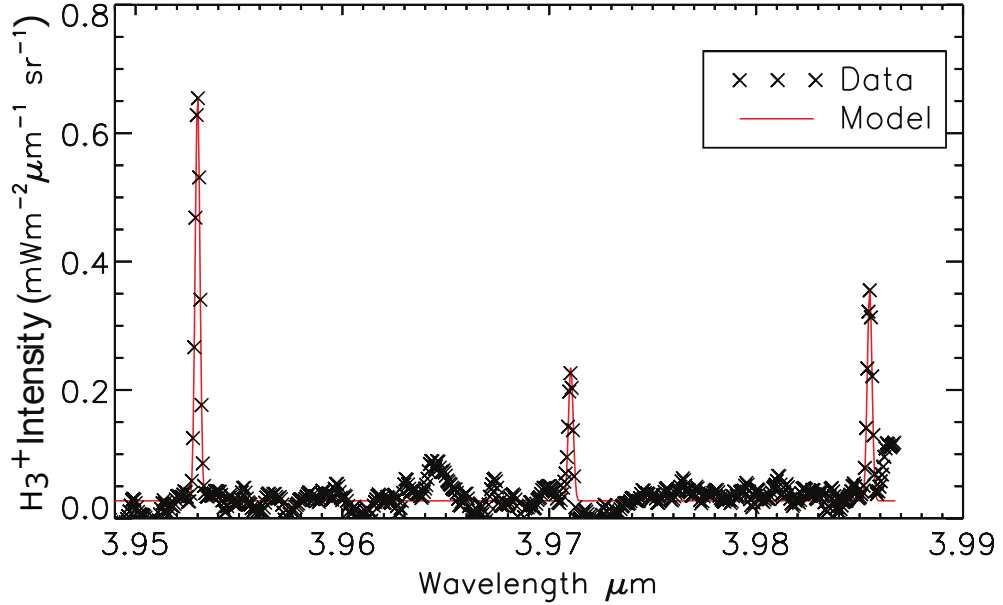


Fig. 5. **Model fit to  $\text{H}_3^+$  intensity as a function of wavelength.** This spectral profile is produced from the co-add of all northern main oval images on April 21 (NMO; 8 - 22° co-latitude). The x- and y-axes show wavelength and intensity of  $\text{H}_3^+$  emission, respectively. The latter is indicated by the black crosses for the observed emission and the model fit to the spectrum is shown in red. The temperature derived for this spectral profile is  $404 \pm 11$  K.

272 figure; Q(1,0<sup>-</sup>), Q(2,1) and Q(3,0). These have transition energies  $\omega$  between upper ( $j$ ) and  
 273 lower ( $i$ ) ro-vibrational energy states of  $\omega_{i,j} = 2529.721 \text{ cm}^{-1}$ ,  $\omega_{i,j} = 2514.619 \text{ cm}^{-1}$  and  $\omega_{i,j} =$   
 274  $2509.074 \text{ cm}^{-1}$ , respectively (further transition line information is available in Table 1 of *Kao*  
 275 *et al.* [1991]). The modeled theoretical spectrum is reproduced for a variety of temperatures  
 276 until a close match is found to the observed spectrum by least-squares fitting. In other words,  
 277 the effective column-integrated temperature of  $\text{H}_3^+$  is found by comparing the observed line  
 278 ratios to model values.

279 Emission by  $\text{H}_3^+$  depends upon its temperature with, in general, a higher temperature lead-  
 280 ing to a spectral transition line of higher intensity. The emission we observe at the detector  
 281 (following the data reduction) is representative of a line-of-sight column-integrated quantity  
 282 of molecules: the column density. Thus by dividing the observed intensity by the intensity of a

283 single molecule we can determine the number of molecules in the column, in units of molecules  
 284 per square metre ( $\text{m}^{-2}$ ).

285 The effective total emission of  $\text{H}_3^+$  is the result of the multiplication of the integrated emission  
 286 per molecule across all wavelengths by the column density, giving a measurement of the total  
 287 emitted power by  $\text{H}_3^+$  as follows [Lam *et al.* 1997]:

$$E(\text{H}_3^+) = E_{mol}(\text{H}_3^+, T) \times N(\text{H}_3^+, T) , \quad (2)$$

288 where  $E_{mol}(\text{H}_3^+, T)$  is the integrated intensity of a  $\text{H}_3^+$  line between 0.75 - 22 microns

$$289 \quad E_{mol}(\text{H}_3^+) = a + bT + cT^2 + dT^3 + eT^4 . \quad (3)$$

290 modeled for a particular temperature,  $T$ . Parameters  $a$  to  $e$  are partition function constants  
 291 detailed and given by Miller *et al.* [2010]. As such, it is a direct measure for the rate of cooling  
 292 of the ionosphere/thermosphere by  $\text{H}_3^+$ , which is itself responsible for some of the cooling in  
 293 the thermosphere [Grodent *et al.* 2001; Raynaud *et al.* 2004; Miller *et al.* 2010].

294 The line-of-sight column density attains a useful physical meaning if it is corrected to the  
 295 altitude of a column that extends vertically from Saturn's surface. Thus each such measurement  
 296 needs to be reduced by some factor dependent upon the angle to the local vertical of the  
 297 observation. Observations by the Cassini spacecraft show that the majority of the  $\text{H}_3^+$  intensity  
 298 is located within the 800 - 1400 km range of altitudes above the 1 bar pressure surface [Stallard  
 299 *et al.* 2012b]. Models are in agreement with this, predicting that the majority of ionospheric  
 300  $\text{H}_3^+$  ions (approximately >90% by number density) are located in this same 600 km range of  
 301 altitudes [e.g. Mueller-Wodarg *et al.* 2012]. By considering two oblate spheroids (with elliptical  
 302 cross-sections) of Saturn tilted at  $18.3^\circ$  relative to the observer, the inner spheroid being the  
 303 1-bar pressure surface of Saturn plus 800 km, and the outer spheroid being at plus 1400 km  
 304 altitude of the same surface, we calculated the depth of the column we observe as a function



305 of latitude. The observed line of sight column of atmosphere becomes larger nearer the poles,  
306 compared to at the equator, and this is corrected for by reducing the measured intensity as a  
307 function of latitude to a normalised value.

308 The spectrum of  $\text{H}_3^+$  can be described as a ‘spectral function’: this function is a sum of  
309 Gaussian fits to all of the ro-vibrational transition lines and depends on the temperature  
310 and density of  $\text{H}_3^+$ . The temperature and density uncertainties from this are found by applying  
311 Cramer’s rule, whilst the uncertainty in total emission is found by using basic error propagation  
312 formulae [see *Melin* 2006; *Melin et al.* 2014, and references therein]. As the temperature and  
313 density parameters are found using a least-squares fit embedded within the  $\text{H}_3^+$  fitting routine,  
314 they are an indicator of the quality of the spectral fit.

315 The most optimal (lowest) seeing achieved herein is  $0.4''$ , which amounts to 2560 km perpen-  
316 dicular to the line-of-sight at a distance of 8.826 astronomical units (the Earth-Saturn distance  
317 on April 20). Therefore, even in the extreme case of a measurement of  $\text{H}_3^+$  on or near the Sat-  
318 urnian limb, we are still capturing the entire column of altitude in which  $\text{H}_3^+$  is distributed  
319 above the 1-bar surface. This means that variability in  $\text{H}_3^+$  parameters that we report herein  
320 should be considered due to variations in latitude and longitude and not in altitude which is  
321 column-integrated at any location.

## 322 4 Results and discussion

323 The total time spent observing in this campaign, including sky exposures of the sky, cali-  
324 brations and general time-overheads (e.g. moving the telescope), was 361 minutes. The total  
325 integration time on Saturn itself was 115 minutes. The exposure times and values of tempera-  
326 ture, column density, and total emission for the northern and southern main ovals (NMO and  
327 SMO) and northern polar cap and midnight oval (NPC and NMMO) are shown in Tables 2,

328 3 and 4 for April 19, 20 and 21, respectively. The start and end universal times (UT) in the  
329 tables correspond to the start of the first Saturn exposure (A frame) and the end of the final  
330 (fifth) A frame; as mentioned earlier, observing time overheads do not permit a continuous  
331 5-minute acquisition.

332 Average parameters for each day are shown in two different ways in this section. The  
333 first is the average of all individually model-fitted spectra for a given parameter over a given  
334 observation night; these are represented by the dashed horizontal lines in each of the figures (6  
335 - 9 inclusive). Note that the values in the first row of Table 2 have unusually high uncertainties,  
336 perhaps due to passing cirrus clouds during the observations; as such, they are not used when  
337 calculating the averages. A second type of averaging, the ‘co-average’, is found by fitting a  
338 model  $H_3^+$  spectrum to the co-addition of all spectral images from each region for each day.  
339 This ensures that the maximum possible S/N is obtained prior to fitting itself. These co-added  
340 averages have higher S/N and lower uncertainty than an individually fitted spectral image and  
341 are given in Tables 2, 3 and 4, although the difference between the two types of averaging are  
342 small.

Start (UT)	End (UT)	$T_{NMO}$ (K)	$T_{NPC}$ (K)	$T_{NMMO}$ (K)	$T_{SMO}$ (K)	$CD_{NMO}$ ( $10^{15} \text{ m}^{-2}$ )	$CD_{NPC}$ ( $10^{15} \text{ m}^{-2}$ )	$CD_{NMMO}$ ( $10^{15} \text{ m}^{-2}$ )	$CD_{SMO}$ ( $10^{15} \text{ m}^{-2}$ )	$E_{NMO}$ ( $10^{-5} \text{ Wm}^{-2} \text{ sr}^{-1}$ )	$E_{NPC}$ ( $10^{-5} \text{ Wm}^{-2} \text{ sr}^{-1}$ )	$E_{NMMO}$ ( $10^{-5} \text{ Wm}^{-2} \text{ sr}^{-1}$ )	$E_{SMO}$ ( $10^{-5} \text{ Wm}^{-2} \text{ sr}^{-1}$ )
10:55	11:18	994 ± 900	925 ± 587	699 ± 212	453 ± 67	0.04 ± 0.06	0.03 ± 0.05	0.03 ± 0.05	0.5 ± 0.5	0.70 ± 0.09	0.37 ± 0.09	0.12 ± 0.02	0.11 ± 0.07
11:23	11:50	389 ± 34	356 ± 32	501 ± 48	466 ± 39	7.4 ± 5.3	10.2 ± 8.6	0.3 ± 0.2	0.7 ± 0.4	0.40 ± 0.37	0.23 ± 0.46	0.14 ± 0.02	0.18 ± 0.03
11:51	12:05	449 ± 38	394 ± 37	506 ± 58	361 ± 30	2.5 ± 1.5	4.1 ± 3.2	0.3 ± 0.2	6.3 ± 4.9	0.46 ± 0.14	0.25 ± 0.21	0.12 ± 0.02	0.17 ± 0.20
12:09	12:22	376 ± 32	496 ± 41	438 ± 50	583 ± 54	10.3 ± 7.8	1.0 ± 0.5	0.7 ± 0.6	0.2 ± 0.1	0.41 ± 0.47	0.39 ± 0.05	0.11 ± 0.05	0.24 ± 0.01
12:23	12:36	396 ± 26	428 ± 32	435 ± 38	498 ± 46	9.0 ± 4.9	2.8 ± 1.6	0.9 ± 0.6	0.5 ± 0.3	0.56 ± 0.25	0.34 ± 0.10	0.13 ± 0.04	0.20 ± 0.03
12:41	12:53	417 ± 32	372 ± 32	471 ± 54	398 ± 51	5.2 ± 3.2	7.8 ± 6.0	0.6 ± 0.5	1.9 ± 2.1	0.52 ± 0.21	0.27 ± 0.31	0.16 ± 0.04	0.13 ± 0.14
12:54	13:07	382 ± 49	451 ± 33	395 ± 34	479 ± 45	11.4 ± 11.4	2.0 ± 1.0	2.1 ± 1.5	0.6 ± 0.4	0.52 ± 0.62	0.38 ± 0.07	0.13 ± 0.08	0.18 ± 0.03
13:11	13:24	407 ± 22	467 ± 38	436 ± 45	444 ± 41	7.9 ± 3.5	1.4 ± 0.8	0.7 ± 0.6	1.0 ± 0.7	0.64 ± 0.17	0.37 ± 0.06	0.10 ± 0.05	0.17 ± 0.05
Co-average*:	402 ± 20	441 ± 16	466 ± 20	442 ± 23	6.4 ± 2.5	2.0 ± 0.5	0.5 ± 0.1	0.9 ± 0.4	0.47 ± 0.02	0.31 ± 0.04	0.12 ± 0.02	0.15 ± 0.03	0.15 ± 0.03
Mean value	404 ± 13	423 ± 13	455 ± 18	460 ± 17	7.7 ± 2.3	4.2 ± 1.6	0.8 ± 0.3	1.5 ± 0.7	0.50 ± 0.12	0.32 ± 0.09	0.13 ± 0.02	0.17 ± 0.03	0.17 ± 0.03

Table 2

Saturn's auroral/polar properties as a function of time on 19 April 2013. All uncertainties shown are one standard deviation (i.e. 1-sigma errors). T, CD and E are temperature, column density and total emission of  $\text{H}_3^+$ , respectively. \*Co-averages are co-add averages formed from applying a model fit to the co-addition of all spectra from the night, rather than of the individual values, whilst the mean values are drawn from the table. Note that the first row is not used in the latter average due to very high uncertainties.

Start (UT)	End (UT)	$T_{NMO}$ (K)	$T_{NPC}$ (K)	$T_{NMMO}$ (K)	$T_{SMO}$ (K)	$CD_{NMO}$ ( $10^{15} \text{ m}^{-2}$ )	$CD_{NPC}$ ( $10^{15} \text{ m}^{-2}$ )	$CD_{NMMO}$ ( $10^{15} \text{ m}^{-2}$ )	$CD_{SMO}$ ( $10^{15} \text{ m}^{-2}$ )	$E_{NMO}$ ( $10^{-5} \text{ Wm}^{-2} \text{ sr}^{-1}$ )	$E_{NPC}$ ( $10^{-5} \text{ Wm}^{-2} \text{ sr}^{-1}$ )	$E_{NMMO}$ ( $10^{-5} \text{ Wm}^{-2} \text{ sr}^{-1}$ )	$E_{SMO}$ ( $10^{-5} \text{ Wm}^{-2} \text{ sr}^{-1}$ )
12:18	12:31	$461 \pm 42$	$426 \pm 35$	$476 \pm 33$	$475 \pm 41$	$2.3 \pm 1.5$	$2.5 \pm 1.6$	$0.7 \pm 0.3$	$0.7 \pm 0.4$	$0.54 \pm 0.13$	$0.31 \pm 0.11$	$0.2 \pm 0.03$	$0.21 \pm 0.03$
12:31	12:46	$476 \pm 37$	$423 \pm 33$	$459 \pm 32$	$460 \pm 32$	$2.1 \pm 1.1$	$2.8 \pm 1.7$	$0.7 \pm 0.4$	$1.1 \pm 0.5$	$0.61 \pm 0.09$	$0.32 \pm 0.11$	$0.15 \pm 0.03$	$0.24 \pm 0.03$
12:51	13:03	$442 \pm 34$	$377 \pm 27$	$439 \pm 31$	$496 \pm 35$	$3.3 \pm 1.9$	$7.1 \pm 4.4$	$1.0 \pm 0.5$	$0.6 \pm 0.3$	$0.53 \pm 0.14$	$0.29 \pm 0.23$	$0.15 \pm 0.03$	$0.23 \pm 0.02$
13:07	13:18	$441 \pm 31$	$503 \pm 37$	$562 \pm 47$	$441 \pm 39$	$3.1 \pm 1.6$	$0.8 \pm 0.4$	$0.2 \pm 0.1$	$1.2 \pm 0.8$	$0.49 \pm 0.13$	$0.34 \pm 0.04$	$0.19 \pm 0.01$	$0.19 \pm 0.05$
Co-average*	$441 \pm 22$	$423 \pm 15$	$471 \pm 17$	$454 \pm 22$	$3.3 \pm 1.3$	$2.8 \pm 0.7$	$0.6 \pm 0.2$	$1.0 \pm 0.4$	$0.54 \pm 0.09$	$0.31 \pm 0.05$	$0.17 \pm 0.01$	$0.22 \pm 0.02$	$0.22 \pm 0.02$
Mean value	$453 \pm 20$	$434 \pm 20$	$487 \pm 22$	$468 \pm 19$	$2.8 \pm 0.9$	$3.6 \pm 1.6$	$0.6 \pm 0.3$	$0.9 \pm 0.3$	$0.54 \pm 0.07$	$0.31 \pm 0.09$	$0.16 \pm 0.02$	$0.22 \pm 0.02$	$0.22 \pm 0.02$

Table 3

As Table 2, but for data obtained on 20 April 2013.

Start (UT)	End (UT)	$T_{NMO}$ (K)	$T_{NPC}$ (K)	$T_{NMMO}$ (K)	$T_{SMO}$ (K)	$CD_{NMO}$ ( $10^{15} \text{ m}^{-2}$ )	$CD_{NPC}$ ( $10^{15} \text{ m}^{-2}$ )	$CD_{NMMO}$ ( $10^{15} \text{ m}^{-2}$ )	$CD_{SMO}$ ( $10^{15} \text{ m}^{-2}$ )	$E_{NMO}$ ( $10^{-5} \text{ Wm}^{-2} \text{ sr}^{-1}$ )	$E_{NPC}$ ( $10^{-5} \text{ Wm}^{-2} \text{ sr}^{-1}$ )	$E_{NMMO}$ ( $10^{-5} \text{ Wm}^{-2} \text{ sr}^{-1}$ )	$E_{SMO}$ ( $10^{-5} \text{ Wm}^{-2} \text{ sr}^{-1}$ )
10:40	10:53	375 ± 18	397 ± 25	525 ± 40	375 ± 30	23.9 ± 10.0	9.6 ± 5.0	0.4 ± 0.2	4.5 ± 3.2	0.89 ± 0.27	0.61 ± 0.14	0.23 ± 0.01	0.17 ± 0.14
10:54	11:07	415 ± 17	387 ± 22	388 ± 34	380 ± 21	9.8 ± 3.2	10.0 ± 5.0	3.6 ± 2.7	6.0 ± 3.0	0.95 ± 0.11	0.51 ± 0.15	0.19 ± 0.09	0.25 ± 0.09
11:12	11:26	384 ± 17	421 ± 21	384 ± 29	398 ± 25	17.3 ± 6.8	5.5 ± 2.1	3.9 ± 2.5	4.3 ± 2.3	0.83 ± 0.21	0.60 ± 0.07	0.18 ± 0.09	0.29 ± 0.07
11:28	11:41	380 ± 17	448 ± 25	393 ± 26	510 ± 36	20.2 ± 7.8	3.4 ± 1.4	3.0 ± 1.7	0.8 ± 0.4	0.87 ± 0.23	0.62 ± 0.06	0.18 ± 0.06	0.39 ± 0.02
11:46	11:59	437 ± 25	506 ± 28	491 ± 43	425 ± 26	5.7 ± 2.4	1.4 ± 0.5	0.7 ± 0.4	2.6 ± 1.2	0.85 ± 0.11	0.67 ± 0.03	0.28 ± 0.02	0.31 ± 0.04
12:00	12:13	364 ± 27	500 ± 35	628 ± 64	495 ± 38	19.1 ± 12.8	1.4 ± 0.6	0.1 ± 0.1	0.6 ± 0.3	0.53 ± 0.53	0.59 ± 0.04	0.24 ± 0.01	0.26 ± 0.02
12:18	12:31	477 ± 35	460 ± 26	439 ± 38	415 ± 28	2.2 ± 1.1	2.7 ± 1.1	1.2 ± 0.8	2.8 ± 1.5	0.68 ± 0.09	0.60 ± 0.05	0.19 ± 0.04	0.27 ± 0.06
12:33	12:46	402 ± 27	407 ± 19	448 ± 32	453 ± 22	8.3 ± 4.5	7.6 ± 2.8	1.1 ± 0.6	2.0 ± 0.7	0.59 ± 0.23	0.62 ± 0.08	0.19 ± 0.03	0.40 ± 0.02
12:51	13:03	391 ± 32	394 ± 26	448 ± 30	452 ± 20	8.3 ± 5.8	9.1 ± 5.1	1.2 ± 0.6	2.0 ± 0.7	0.46 ± 0.35	0.54 ± 0.16	0.21 ± 0.03	0.41 ± 0.02
13:05	13:18	423 ± 29	485 ± 29	495 ± 37	436 ± 22	5.3 ± 2.9	1.9 ± 0.8	0.6 ± 0.3	2.6 ± 1.0	0.60 ± 0.17	0.64 ± 0.04	0.23 ± 0.02	0.37 ± 0.03
13:23	13:36	420 ± 32	505 ± 28	483 ± 46	512 ± 33	4.9 ± 2.9	1.5 ± 0.5	0.5 ± 0.3	0.8 ± 0.3	0.52 ± 0.19	0.69 ± 0.03	0.17 ± 0.03	0.38 ± 0.02
Co-average*	404 ± 11	436 ± 9	460 ± 11	436 ± 10	9.2 ± 2.1	4.0 ± 0.6	0.9 ± 0.2	2.1 ± 0.4	0.70 ± 0.09	0.60 ± 0.02	0.20 ± 0.01	0.31 ± 0.01	0.31 ± 0.01
Mean value	409 ± 8	451 ± 9	460 ± 12	441 ± 9	10.1 ± 1.9	4.5 ± 0.8	1.6 ± 0.4	2.6 ± 0.5	0.70 ± 0.08	0.61 ± 0.03	0.21 ± 0.02	0.32 ± 0.02	0.32 ± 0.02

Table 4

As Table 2, but for data obtained on 21 April 2013.

344 In Tables 2 - 4, the co-added average temperatures in the NMO are lower than in the SMO  
 345 on each day. The individually derived  $\text{H}_3^+$  temperatures for the spectral images are shown in  
 346 Figure 6, together with dashed lines which indicate the average value of all of the data points  
 347 (i.e. not the same averages as in Tables 2 - 4, but the differences between the two are very  
 348 small). *O'Donoghue et al.* [2014] found that over a period of  $\sim 2$  hours the southern main  
 349 auroral oval was on average 56 K hotter than its northern counterpart. This was attributed  
 350 to the north-south asymmetry in magnetic field strength which leads to an overall larger total  
 351 heating rate in the south, with the caveat being that their dataset was small and considered a  
 352 snapshot of events at that time (in April 2011). In this work we have three similar snapshots  
 353 over consecutive days, each appearing to support to the previous result that the SMO is warmer  
 354 than the NMO by 10's of K when measured simultaneously for each of the days.

355 A summary of the effective average  $\text{H}_3^+$  temperatures observed to date is presented in Table  
 356 5. The considerable year-to-year variability is difficult to attribute to seasonal or solar cycle  
 357 effects, such that variability on shorter time scales of minutes, hours, and days should be  
 358 considered. This is discussed in Subsection 4.3 where we outline a likely reason for the several  
 359 10's of Kelvin variability seen in the NMO temperatures.

360 Tables 2 - 4 also show that column densities are higher in the northern main oval than  
 361 the southern by on average a factor of  $\sim 3$ , as shown in Figure 7, though these have large  
 362 uncertainties associated with them. A possible reason for a higher northern column density is  
 363 the additional solar illumination in the north compared with that incident at the south; this  
 364 yields a higher ionisation rate of  $\text{H}_2$  and therefore an increase in  $\text{H}_3^+$  production. Such an effect  
 365 has previously been observed and also demonstrated using the 1-D Saturn Thermosphere Iono-  
 366 sphere Model (STIM) by *O'Donoghue et al.* [2014]. All but one pair of values is in agreement

Date	$T_{SMO}$ (K)	$T_{NMO}$ (K)	$T_{NPC}$ (K)	$T_{NMMO}$ (K)	Source
Sept. 1999	$380 \pm 70$	-	-	-	NASA IRTF, <i>Melin et al.</i> [2007]
Feb. 2004	$420 \pm 70$	-	-	-	NASA IRTF, <i>Melin et al.</i> [2007]
July 2007	$590 \pm 50$	-	-	-	Cassini VIMS, <i>Stallard et al.</i> [2012a]
Jan. 2009	$410 \pm 85$	-	-	-	Cassini VIMS, <i>Lamy et al.</i> [2013]
April 2011	$583 \pm 13$	$527 \pm 18$	-	-	Keck, <i>O'Donoghue et al.</i> [2014]
April 2013	$444 \pm 18$	$416 \pm 18$	$433 \pm 13$	$466 \pm 16$	Keck, This work

Table 5

The average temperatures of Saturn's auroral regions obtained between 1999 and the 2013.

367 with this trend; at  $\sim 12$  UT on April 19 in panel (a) the southern column density is higher.  
368 The densities vary by up to an order of magnitude from day-to-day, with the major deviations  
369 outside the ranges of uncertainty seen in panel (c).

370 The variability in column density is likely to be associated with changes in the energy flux  
371 that is incident on the ionosphere, e.g. increased particle precipitation provides more ionization  
372 and thus more  $H_3^+$ . Similar variability in the energy flux has been attributed to variations in  
373  $H_3^+$  aurora before using Cassini VIMS data [*Badman et al.* 2012b;a], and in patches of intense  
374 UV emissions from H and  $H_2$  [*Nichols et al.* 2009; *Grodent et al.* 2011; *Meredith et al.* 2013]. An  
375 influx of particles at local noon may be the result of dayside reconnection events which occur  
376 when the interplanetary magnetic field (IMF) is orientated northward, leading to the opening  
377 of closed planetary magnetic field lines to the solar wind, causing a planetward influx of solar  
378 particles [*Radioti et al.* 2011; 2013; *Badman et al.* 2013; *Meredith et al.* 2014; *Belenkaya et al.*  
379 2014]. Alternatively, new parts of the main auroral oval, differing in their levels of activity, may  
380 be rotating into view on the spectrograph slit. No correlations are found between the northern  
381 and southern main ovals, despite sharing common (closed) magnetic field lines, and this is  
382 consistent with recent Hubble Space Telescope (HST) observations which showed patches of  
383 UV emission in the auroral main oval are present in one hemisphere, but absent from the

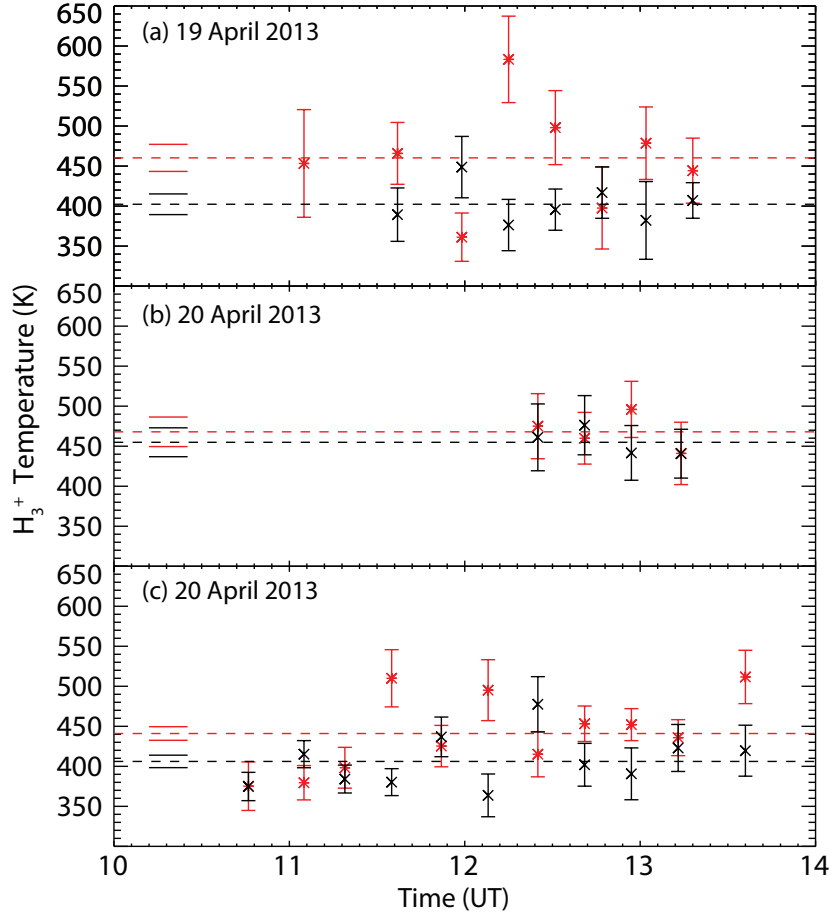


Fig. 6. NMO and SMO  $H_3^+$  temperature as a function of observation time. The three panels show  $H_3^+$  temperatures as a function of time for the three nights of observations as indicated. The NMO values are shown as the black crosses, while the SMO values are shown as the red asterisks. The uncertainties listed are 1-sigma and arise from the S/N of the spectral fit. Note that the northern main oval temperature of  $994 \pm 900$  K (in the first row of Table 2) is not shown in panel (a), as it is assumed to be unphysical (this was possibly due to a passing cirrus cloud, reducing the S/N). The black and red dashed horizontal lines show the average temperature of all the plotted data points for north and south, respectively, with associated 1-sigma uncertainties above and below shown as short solid lines.

384 magnetically conjugate location in the other [Meredith *et al.* 2014].

385 The total emission shown in Tables 2 - 4 and Figure 8 is higher in the NMO for nearly all  
 386 data points compared to the SMO - a similar trend is seen in column density, but in this case



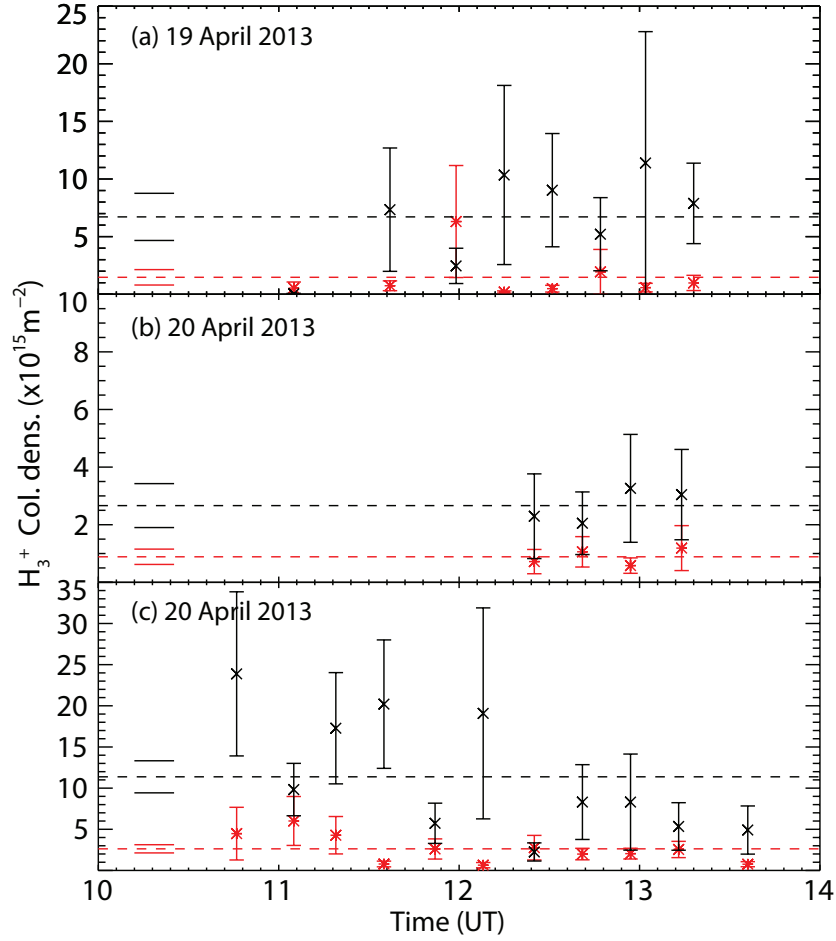


Fig. 7. NMO and SMO  $H_3^+$  column densities as a function of time. The figure format is the same as Figure 6.

387 with smaller uncertainties. The total emission is a direct measure of  $H_3^+$  cooling to space, so it  
 388 might be argued that in the NMO, the larger quantity of  $H_3^+$  would have led to a higher rate of  
 389 thermospheric cooling, which in turn has led to lower temperatures. However, the observations  
 390 by *O'Donoghue et al.* [2014] are a counter example in that high densities are associated with low  
 391 total emissions, so this is not an obvious cause. Furthermore, the global circulation modeling  
 392 (GCM) results of *Mueller-Wodarg et al.* [2012] of Saturn during equinoctial conditions show  
 393 that  $H_3^+$  acts only as a minor coolant in the thermosphere. The major heating mechanism  
 394 in the auroral thermosphere is Joule heating, whilst adiabatic cooling and advection are the  
 395 major heat sinks in the upper polar atmosphere. The densities observed here are similar to  
 396 *O'Donoghue et al.* [2014] and are within the 1 to  $12 \times 10^{15} \text{m}^{-2}$  range of values modeled by

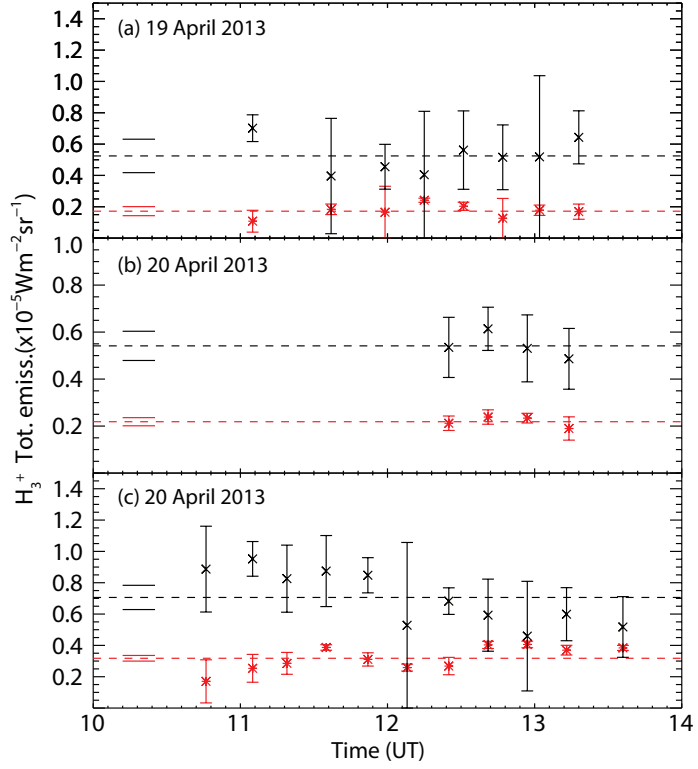


Fig. 8. NMO and SMO  $H_3^+$  total emission as a function of time. The figure format is the same as Figure 6.

397 *Mueller-Wodarg et al.* [2012]. There are no obvious trends found here that lead us to conclude  
 398 a dependence of  $H_3^+$  parameters with system III CML. The NMO and SMO individually show  
 399 sporadic variability of several 10's of K throughout all CML's, indicating little or no observable  
 400 relationship.

402 In Figure 9 we show the  $H_3^+$  parameters of all of the four previously mentioned spatial  
403 regions (as shown in Figure 3) as a function of system III longitude (CML). Before continuing  
404 we note that the nearby components of the north are close together and therefore subject to  
405 latitudinal smearing, i.e. cross-contamination, even though gaps were left between the target  
406 areas. This is due to (mainly) atmospheric scintillation/seeing effects and telescope movement  
407 during spectral image exposures. However, comparison between the northern main oval and  
408 midnight are separated significantly enough that these effects are negligible. First, we find that  
409 there are no obvious trends leading us to conclude a dependence of  $H_3^+$  parameters with CML.  
410 The northern and southern main ovals individually show sporadic variability of several 10's of  
411 K throughout all CMLs, indicating little or no observable relationship. However, the northern  
412 main oval (black crosses) total emission and column density do appear to have significantly  
413 higher values than the average near 50-100° CML, and this will be discussed in the next section.  
414 A lack of an obvious pattern is perhaps unsurprising as there are no known CML dependencies  
415 of Saturn's magnetic field. Our interests here therefore lie mainly in the average behavior of  
416 each region from the combined three days of observations. The CMLs for the northern midnight  
417 main oval are shifted by 180 degrees as they are on the 'night' (but sunlit) side of the planet,  
418 whilst the northern polar cap (which straddles both sides) uses northern main oval CMLs. The  
419 effective column integrated  $H_3^+$  temperature is on average 465 K at midnight, 53 K greater than  
420 in the main oval. Column density averages are  $1 \times 10^{15} \text{ m}^{-2}$  at midnight and  $8.6 \times 10^{15} \text{ m}^{-2}$  at  
421 noon, similar to values produced through modeling efforts by *Moore et al.* [2004], though these  
422 were produced by solar EUV alone (i.e., non-auroral conditions). Finally, the total emission  
423 is  $0.6 \times 10^{-5} \text{ Wm}^{-2}\text{sr}^{-1}$  at noon and  $0.18 \times 10^{-5} \text{ Wm}^{-2}\text{sr}^{-1}$  at northern midnight. The polar  
424 aurora temperature is 439 K on average, whilst the column density and total emission values  
425 are 45% and 75%, respectively, of the northern main oval values, indicating that perhaps this

426 region is contaminated by its neighbors through the seeing effects mentioned above. Southern  
 427 parameters have already been discussed in the context of their northern counterparts, but  
 428 appear to be most similar to the northern midnight main oval.

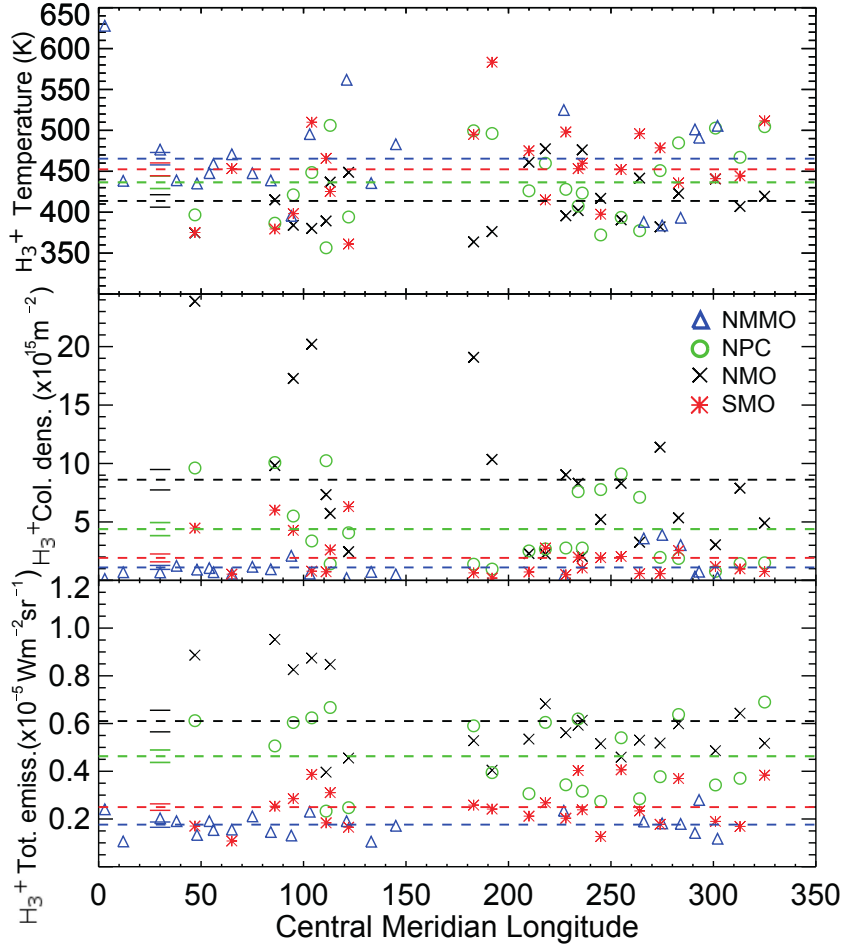


Fig. 9. Northern  $\text{H}_3^+$  properties as a function of Saturn system III CML. Here we show the northern  $\text{H}_3^+$  temperature, column density and total emission in panels (a), (b) and (c), respectively as a function of central meridian longitude. The different regions of interest are the northern main oval (black crosses), polar cap (green circles), midnight aurorae (blue triangles) and southern main oval (red asterisks). The average values for each are shown as dashed horizontal lines with 1-sigma uncertainty bars as short solid lines above and below to the left of the figure. The northern values at  $\sim 62^\circ$  CML are not shown and not included in the calculation of average values due to high uncertainties described earlier.

429 *Mueller-Wodarg et al.* [2012] modeled Saturn's upper atmosphere for equinoctial conditions,  
430 including the effects of solar radiation, magnetospheric electron precipitation and the contribu-  
431 tion to the total heating rate provided by Joule heating and ion drag. The authors calculated  
432 auroral  $\text{H}_3^+$  temperatures (at  $78^\circ$  southern latitude) of  $\sim 419$  K at midnight, 1 - 2 K warmer  
433 than at noon. Although these temperatures are similar in absolute terms to those observed in  
434 this work, the difference between the noon and midnight sectors is clearly much greater here  
435 (55 K); the reason for this midnight temperature enhancement is unknown. The column den-  
436 sity, on the other hand, was modeled to be  $\sim 12 \times 10^{15} \text{ m}^{-2}$  at noon, compared with  $\sim 1 \times 10^{15}$   
437  $\text{m}^{-2}$  at midnight, similar to that observed here. The northern column emission is a factor of  
438  $\sim 3$  higher at noon compared to midnight in our observations, yet a factor of 15 different in the  
439 above model. There are thus some areas of agreement between the model of *Mueller-Wodarg*  
440 *et al.* [2012] and the observations presented here, though the relative noon-midnight differences  
441 between parameters are quite large. Cross-contamination between the polar cap and the main  
442 oval due to atmospheric seeing may play a role in the observation-model factor differences  
443 between noon and midnight. The higher noon density and emission is likely to be driven by  
444 the higher levels of 10 keV electron flux there, in accordance with the predicted maximum  
445 flux at 08:00 Saturn local time (SLT), which then diminishes to a minimum near midnight  
446 [*Lamy et al.* 2009]. The parameters obtained in the polar region shown by the green circles in  
447 Figure 9 appear essentially to be the average of the other northern values. The activity here  
448 could be maintained by transport from the midnight and noon sectors, as well as be modulated  
449 by particle precipitation along open field lines which connect the planet directly to the solar  
450 wind.

452 In the last section, although there was no clear organisation with CML, there were a number  
453 of high density and emission values in the northern main oval at around 50-100° CML in Figure  
454 9. In addition, this is a region in which we have a complete view of the 8 - 20° co-latitudes that  
455 define it (compared with the limited southern main oval field of view of 18 - 22° ), so it is an  
456 ideal place to explore any short-term variability; in particular, that imposed by the planetary  
457 period oscillations of the magnetic field. In the four panels of Figure 10 we plot each of the  
458 NMO  $H_3^+$  parameters from all three days as a function of PPO phase,  $\Psi_N$ , between 0° and  
459 360°. In Figure 10 panel (a) we plot the  $H_3^+$  Q(1,0) line intensity versus the northern PPO  
460 phase, and we find a factor of  $\sim 2$  higher intensity between 90 - 135°. The line intensity is a  
461 useful metric for the overall activity of  $H_3^+$  as it is directly observed and is a function of both  
462 temperature and density. The location of the center of the fitted Gaussian distribution curve  
463 (the peak) shown over-plotted in black is located at 115° and has a FWHM of 44°. Figure 10  
464 panel (b) shows the NMO temperature against northern PPO phase, and this anti-correlates  
465 with the column density shown in panel (c) with a Spearman's rank coefficient  $r = -0.95$   
466 (with a probability that these values are uncorrelated of  $p < 0.01$ ). This and other correlations  
467 between  $H_3^+$  parameters are given in Table 6. The column density Gaussian curve peaks at  
468 118° and has a FWHM of 49°- almost identical in location to the Q(1,0) line peak. In panel  
469 (d) the total emission the Gaussian curve peaks at 114° with a FWHM of 40°.

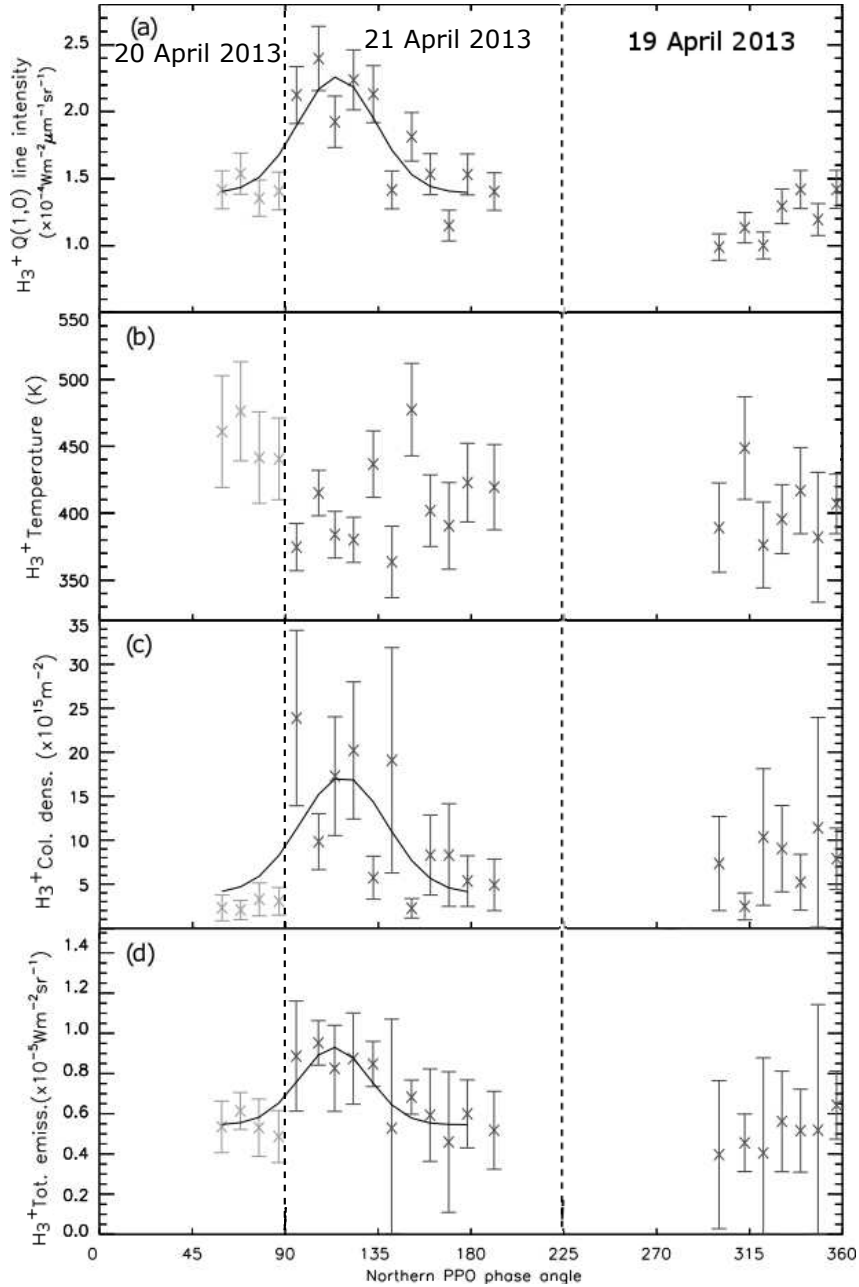


Fig. 10. NMO  $\text{H}_3^+$  parameters as a function of northern PPO phase. Here we show the northern main oval results from the three days of this study as a function of the PPO phase angle described in the main text. The following  $\text{H}_3^+$  parameters are shown in each of the four panels: (a) Q(1,0) line intensity, (b) temperature, (c) column density and (d) total emission.

470 The theoretical peak particle precipitation is thought to occur at  $\Psi_N = 90^\circ$  as discussed  
 471 in the introduction, so the above locations are some 25 degrees later on in PPO phase (1  
 472 hour and 40 minutes earlier in Saturn LT). First we note that the phase model is accurate to

H <sub>3</sub> <sup>+</sup> parameter	Temperature	Column density	Total emission
Q(1,0) intensity	$r = -0.04$ ( $p = 0.85$ )	$r = 0.25$ ( $p = 0.23$ )	$r = -0.79$ ( $p < 0.01$ )
Total emission	$r = 0.08$ ( $p = 0.73$ )	$r = 0.17$ ( $p = 0.43$ )	-
Column density	$r = -0.95$ ( $p < 0.01$ )	-	-

Table 6

Spearman's rank correlation coefficients between H<sub>3</sub><sup>+</sup> parameters when arranged in order of PPO phase.

473 approximately  $\pm 10^\circ$ , so this may account for some of the deviation from expectations [*Provan*  
474 *et al.* 2014]. Second, the FWHM is approximately  $44^\circ$  for the peaks above, a considerable spread  
475 in longitude; a reason for this may be the fact that our measurements are based on spectral  
476 image exposures that are  $\sim 15$  minutes in length and thus accuracy is limited to approximately  
477  $\pm 5^\circ$  in PPO phase. Finally, the position of the starting location/time of the measured peak  
478 in density and emission could be shifted forward due to the chemical lifetime of H<sub>3</sub><sup>+</sup> being  
479 approximately 100 - 1000 seconds [*Badman et al.* 2014]. The lifetime of H<sub>3</sub><sup>+</sup> is also likely to  
480 extend the end location/time of the Gaussian profile. Here by combining the recombination  
481 rate  $17.32 \times 10^{-7} \text{cm}^3 \text{s}^{-1}$  from *Moses and Bass* [2000] with typical values for the temperature  
482 and number density in the auroral region at these altitudes, 450 K and  $1 \times 10^4 \text{cm}^{-3}$  [*Mueller-*  
483 *Wodarg et al.* 2012], we obtain an H<sub>3</sub><sup>+</sup> lifetime of  $\sim 1230$  seconds. These factors when combined  
484 could result in the Gaussian profile being shifted by up to 20 degrees CML/phase angle later,  
485 so the results herein are not inconsistent with the predicted periodic enhancement in electron  
486 influx.

487 We have indicated the results from different days in the panels of Figure 10. The majority  
488 of the curvature of the profile coming from the data taken on 21 April. As this dataset has  
489 no overlapping PPO phase data from the different days, we cannot rule out that the observed  
490 patterns are due to an enhancement in particle precipitation driven by other mechanisms.  
491 For example, an interplanetary magnetic field (IMF) pointing northward can lead to magnetic



492 reconnection at low latitudes, such that planetary field lines become open and connect with  
493 the solar wind [*Badman et al.* 2013]. A combination of longer observations and overlapping  
494 data over the same PPO phases are required in order to definitively confirm the findings here.

495 Interestingly, the temperature appears to be lowest where the influx of charged particles is  
496 highest. This could be in part due to a slight cooling effect of  $\text{H}_3^+$  whereby it radiates heat to  
497 space, although modeling work has shown such cooling is minor compared to other processes  
498 like adiabatic cooling [*Mueller-Wodarg et al.* 2012]. Given the uncertainties in column density,  
499 it is possible that the anti-correlations are not entirely physical and are tainted by the least-  
500 squares fitting routine employed herein [*Melin et al.* 2014]. However, the trends in Figure  
501 10 are arrived at independently from the fitting routine in panel (a) and through a combined  
502 temperature and column density in panel (d), thus we have shown multiple instances of possible  
503  $\text{H}_3^+$ -PPO phase dependence.

504 Analysis of the other regions (SMO, NPC, NMMO) did not yield similar correlations (or at  
505 least, not as strongly) to that of the NMO, although those are regions of lower spatial resolution  
506 and higher cross-latitude contamination due to seeing effects. Given the significant variability  
507 seen here, it is important that similar future research include the contributions made by the  
508 PPO perturbation.

## 509 **5 Summary**

510 On April 19, 20 and 21, the ground-based Keck telescope was employed to simultaneously  
511 measure  $\text{H}_3^+$  parameters (temperature, density and total emission) in four specific regions of  
512 Saturn's ionosphere/thermosphere: 1) the northern noon region of the main auroral oval; 2) the  
513 northern midnight main oval; 3) the northern polar cap and 4) the southern noon main oval. In  
514 these locations, the 115 minutes of captured exposures on Saturn were used to derive ninety-two

515  $\text{H}_3^+$  temperatures, column densities and total emissions spread over timescales of both hours and  
516 days, and therefore over a wide range of Saturn system III longitudes (CMLs) and planetary  
517 period oscillation (PPO) phase angles. We have found that column integrated thermospheric  
518 temperatures in the northern main oval are cooler than their southern counterparts by tens  
519 of K on average. Although the northern aurorae is at times hotter than the south for some  
520 individual measurements, this work lends support the hypothesis that the total thermospheric  
521 heating rate (Joule heating and ion drag) is inversely proportional to magnetic field strength,  
522 as discussed by *O'Donoghue et al.* [2014]. The midnight portion of the oval is on average 55 K  
523 warmer than it is at noon, but the cause for this is unclear. The main oval column integrated  $\text{H}_3^+$   
524 density and emission is lower at northern midnight than it is at noon, in agreement with a peak  
525 in the electron influx at 08:00 Saturn local time and a minimum flux at midnight. When the  
526 northern main oval parameters of  $\text{H}_3^+$  are ordered into the northern PPO phase we see a large  
527 peak in  $\text{H}_3^+$  density and emission at  $\sim 115^\circ$  northern phase, with a full-width at half-maximum  
528 (FWHM) of  $\sim 44^\circ$ . We find that these peaks are most likely due to the expected theoretical  
529 enhancement in the influx of electrons associated with the PPO phase at  $90^\circ$ . A combination  
530 of the  $\text{H}_3^+$  reaction time to the influx due to ion chemistry timescales, the  $\pm 10^\circ$  uncertainty in  
531 the location of a given PPO phase and the lifetime of  $\text{H}_3^+$  are likely to be partly responsible  
532 for the observed peaks in  $\text{H}_3^+$  density and emission occurring later in time (forward in phase)  
533 of the expected precipitation location.

534 **Acknowledgements** The data presented herein were obtained at the W.M. Keck Observa-  
535 tory, which is operated as a scientific partnership among the California Institute of Technology,  
536 the University of California, and NASA. We are particularly grateful to the observing staff in  
537 both Waimea and Mauna Kea for their kind assistance and we praise their ability to seem-  
538 ingly clear the sky of clouds whenever we observe. The observations were made to support the  
539 Cassini auroral campaign in April 2013. Discussions within the international team lead by Tom  
540 Stallard on ‘Comparative Jovian Aeronomy’ have greatly benefited this work; this was hosted

541 by the International Space Science Institute (ISSI). The UK Science and Technology Facili-  
542 ties Council (STFC) supported this work through the Studentship Enhancement Programme  
543 (STEP) for J.O'D. and consolidated grant support for T.S.S., S.W.H.C. and H.M., whilst  
544 S.V.B. was supported by a Royal Astronomical Society Research Fellowship. This material  
545 is based upon work supported by the National Aeronautics and Space Administration under  
546 Grant No. 9500303356 issued through the Planetary Astronomy Program for L.M. and J.O'D.  
547 We thank the NASA Planetary Data System (PDS) for planetary parameter and viewing  
548 geometry data.

## 549 References

- 550 Andrews, D. J., E. J. Bunce, S. W. H. Cowley, M. K. Dougherty, G. Provan, and D. J. South-  
551 wood (2008), Planetary period oscillations in Saturn's magnetosphere: Phase relation of  
552 equatorial magnetic field oscillations and Saturn kilometric radiation modulation, *J. Geo-*  
553 *phys. Res. (Space Physics)*, *113*, A09205, doi:10.1029/2007JA012937.
- 554 Andrews, D. J., A. J. Coates, S. W. H. Cowley, M. K. Dougherty, L. Lamy, G. Provan, and  
555 P. Zarka (2010), Magnetospheric period oscillations at Saturn: Comparison of equatorial  
556 and high-latitude magnetic field periods with north and south Saturn kilometric radiation  
557 periods, *J. Geophys. Res. (Space Physics)*, *115*, A12252, doi:10.1029/2010JA015666.
- 558 Badman, S. V., S. W. H. Cowley, J.-C. Gérard, and D. Grodent (2006), A statistical analysis  
559 of the location and width of Saturn's southern auroras, *Ann. Geophys.*, *24*, 3533–3545, doi:  
560 10.5194/angeo-24-3533-2006.
- 561 Badman, S. V., D. J. Andrews, S. W. H. Cowley, L. Lamy, G. Provan, C. Tao, S. Kasahara,  
562 T. Kimura, M. Fujimoto, H. Melin, T. Stallard, R. H. Brown, and K. H. Baines (2012a),  
563 Rotational modulation and local time dependence of Saturn's infrared  $H_3^+$  auroral intensity,  
564 *J. Geophys. Res.*, *117*, A09228, doi:10.1029/2012JA017990.
- 565 Badman, S. V., N. Achilleos, C. S. Arridge, K. H. Baines, R. H. Brown, E. J. Bunce, A. J.

566 Coates, S. W. H. Cowley, M. K. Dougherty, M. Fujimoto, G. Hospodarsky, S. Kasahara,  
567 T. Kimura, H. Melin, D. G. Mitchell, T. Stallard, and C. Tao (2012b), Cassini observations of  
568 ion and electron beams at Saturn and their relationship to infrared auroral arcs, *J. Geophys.*  
569 *Res.*, *117*, A01211, doi:10.1029/2011JA017222.

570 Badman, S. V., A. Masters, H. Hasegawa, M. Fujimoto, A. Radioti, D. Grodent, N. Sergis,  
571 M. K. Dougherty, and A. J. Coates (2013), Bursty magnetic reconnection at Saturn's mag-  
572 netopause, *Geophys. Res. Lett.*, *40*, 1027–1031, doi:10.1002/grl.50199.

573 Badman, S. V., G. Branduardi-Raymont, M. Galand, S. L. G. Hess, N. Krupp, L. Lamy,  
574 H. Melin, and C. Tao (2014), Auroral Processes at the Giant Planets: Energy Deposition,  
575 Emission Mechanisms, Morphology and Spectra, *Space Sci. Rev.*, doi:10.1007/s11214-014-  
576 0042-x.

577 Barrow, D. J., and K. I. Matcheva (2013), Modeling the effect of atmospheric gravity waves  
578 on Saturn's ionosphere, *Icarus*, *224*, 32–42, doi:10.1016/j.icarus.2013.01.027.

579 Belenkaya, E. S., S. W. H. Cowley, C. J. Meredith, J. D. Nichols, V. V. Kalegaev, I. I. Alexeev,  
580 O. G. Barinov, W. O. Barinova, and M. S. Blokhina (2014), Magnetospheric magnetic field  
581 modelling for the 2011 and 2012 HST Saturn aurora campaigns - implications for auroral  
582 source regions, *Ann. Geophys.*, *32*, 689–704, doi:10.5194/angeo-32-689-2014.

583 Brown, R. H., K. H. Baines, G. Bellucci, J.-P. Bibring, B. J. Buratti, F. Capaccioni, P. Cer-  
584 roni, R. N. Clark, A. Coradini, D. P. Cruikshank, P. Drossart, V. Formisano, R. Jaumann,  
585 Y. Langevin, D. L. Matson, T. B. McCord, V. Mennella, E. Miller, R. M. Nelson, P. D.  
586 Nicholson, B. Sicardy, and C. Sotin (2004), The Cassini Visual And Infrared Mapping Spec-  
587 trometer (Vims) Investigation, *Space Science Reviews*, *115*, 111–168, doi:10.1007/s11214-  
588 004-1453-x.

589 Bunce, E. J., C. S. Arridge, J. T. Clarke, A. J. Coates, S. W. H. Cowley, M. K. Dougherty,  
590 J.-C. Gérard, D. Grodent, K. C. Hansen, J. D. Nichols, D. J. Southwood, and D. L. Talboys  
591 (2008), Origin of Saturn's aurora: Simultaneous observations by Cassini and the Hubble  
592 Space Telescope, *J. Geophys. Res. (Space Physics)*, *113*, A09209, doi:10.1029/2008JA013257.

593 Burton, M. E., M. K. Dougherty, and C. T. Russell (2010), Saturn’s internal planetary magnetic  
594 field, *J. Geophys. Res.*, *37*, L24105, doi:10.1029/2010GL045148.

595 Carbary, J. F. (2012), The morphology of Saturn’s ultraviolet aurora, *J. Geophys. Res. (Space*  
596 *Physics)*, *117*, A06210, doi:10.1029/2012JA017670.

597 Cowley, S. W. H., and E. J. Bunce (2003), Corotation-driven magnetosphere-ionosphere cou-  
598 pling currents in Saturn’s magnetosphere and their relation to the auroras, *Annales Geo-*  
599 *physicae*, *21*, 1691–1707, doi:10.5194/angeo-21-1691-2003.

600 Cowley, S. W. H., E. J. Bunce, and J. M. O’Rourke (2004), A simple quantitative model  
601 of plasma flows and currents in Saturn’s polar ionosphere, *J. Geophys. Res.*, *109*, A05212,  
602 doi:10.1029/2003JA010375.

603 Grodent, D., J. H. Waite, Jr., and J.-C. Gérard (2001), A self-consistent model of the Jovian  
604 auroral thermal structure, *J. Geophys. Res.*, *106*, 12,933–12,952, doi:10.1029/2000JA900129.

605 Grodent, D., J. Gustin, J.-C. Gérard, A. Radioti, B. Bonfond, and W. R. Pryor (2011),  
606 Small-scale structures in Saturn’s ultraviolet aurora, *J. Geophys. Res. (Space Physics)*, *116*,  
607 A09225, doi:10.1029/2011JA016818.

608 Gurnett, D. A., A. Lecacheux, W. S. Kurth, A. M. Persoon, J. B. Groene, L. Lamy, P. Zarka,  
609 and J. F. Carbary (2009), Discovery of a north-south asymmetry in Saturn’s radio rotation  
610 period, *Geophys. Res. Lett.*, *36*, L16102, doi:10.1029/2009GL039621.

611 Hunt, G. J., S. W. H. Cowley, G. Provan, E. J. Bunce, I. I. Alexeev, E. S. Belenkaya, V. V. Kale-  
612 gaev, M. K. Dougherty, and A. J. Coates (2014), Field-aligned currents in Saturn’s southern  
613 nightside magnetosphere: Sub-corotation and planetary period oscillation components., *J.*  
614 *Geophys. Res. (submitted)*.

615 Kaiser, M. L., M. D. Desch, J. W. Warwick, and J. B. Pearce (1980), Voyager de-  
616 tection of nonthermal radio emission from Saturn, *Science*, *209*, 1238–1240, doi:  
617 10.1126/science.209.4462.1238.

618 Kao, L., T. Oka, S. Miller, and J. Tennyson (1991), A table of astronomically important ro-  
619 vibrational transitions for the H<sub>3</sub>(+) molecular ion, *ApJS*, *77*, 317–329, doi:10.1086/191606.

620 Koskinen, T. T., B. R. Sandel, R. V. Yelle, F. J. Capalbo, G. M. Holsclaw, W. E. Mc-  
621 Clintock, and S. Edgington (2013), The density and temperature structure near the  
622 exobase of Saturn from Cassini UVIS solar occultations, *Icarus*, *226*, 1318–1330, doi:  
623 10.1016/j.icarus.2013.07.037.

624 Lam, H. A., N. Achilleos, S. Miller, J. Tennyson, L. M. Trafton, T. R. Geballe, and G. E.  
625 Ballester (1997), A Baseline Spectroscopic Study of the Infrared Auroras of Jupiter, *Icarus*,  
626 *127*, 379–393, doi:10.1006/icar.1997.5698.

627 Lamy, L., B. Cecconi, R. Prangé, P. Zarka, J. D. Nichols, and J. T. Clarke (2009), An auroral  
628 oval at the footprint of Saturn’s kilometric radio sources, colocated with the UV aurorae, *J.*  
629 *Geophys. Res. (Space Physics)*, *114*, A10212, doi:10.1029/2009JA014401.

630 Lamy, L., R. Prangé, W. Pryor, J. Gustin, S. V. Badman, H. Melin, T. Stallard, D.-G.  
631 Mitchell, and P. C. Brandt (2013), Multispectral simultaneous diagnosis of Saturn’s au-  
632 rorae throughout a planetary rotation, *J. Geophys. Res. (Space Physics)*, *118*, 4817–4843,  
633 doi:10.1002/jgra.50404.

634 McLean, I. S., E. E. Becklin, O. Bendiksen, G. Brims, J. Canfield, D. F. Figer, J. R. Graham,  
635 J. Hare, F. Lacayanga, J. E. Larkin, S. B. Larson, N. Levenson, N. Magnone, H. Teplitz, and  
636 W. Wong (1998), Design and development of NIRSPEC: a near-infrared echelle spectrograph  
637 for the Keck II telescope, in *Society of Photo-Optical Instrumentation Engineers (SPIE)*  
638 *Conference Series, Society of Photo-Optical Instrumentation Engineers (SPIE) Conference*  
639 *Series*, vol. 3354, edited by A. M. Fowler, pp. 566–578.

640 Melin, H. (2006), Comparative Aeronomy of the Upper Atmospheres of the Giant Planets,  
641 *University College London*.

642 Melin, H., S. Miller, T. Stallard, L. M. Trafton, and T. R. Geballe (2007), Variability in the  $H_3^+$   
643 emission of Saturn: Consequences for ionisation rates and temperature, *Icarus*, *186*, 234–241,  
644 doi:10.1016/j.icarus.2006.08.014.

645 Melin, H., T. Stallard, S. Miller, J. Gustin, M. Galand, S. V. Badman, W. R. Pryor,  
646 J. O’Donoghue, R. H. Brown, and K. H. Baines (2011), Simultaneous Cassini VIMS

647 and UVIS observations of Saturn’s southern aurora: Comparing emissions from H, H<sub>2</sub>  
648 and H<sub>3</sub><sup>+</sup> at a high spatial resolution, *Geophysical Research Letters*, *38*, L15203, doi:  
649 10.1029/2011GL048457.

650 Melin, H., T. S. Stallard, J. O’Donoghue, S. V. Badman, S. Miller, and J. S. D. Blake (2014),  
651 On the anticorrelation between H<sub>3</sub><sup>+</sup> temperature and density in giant planet ionospheres,  
652 *Mon. Not. R. Astron. Soc.*, *438*, 1611–1617, doi:10.1093/mnras/stt2299.

653 Meredith, C., S. W. H. Cowley, K. C. Hansen, J. D. Nichols, and T. K. Yeoman (2013),  
654 Simultaneous conjugate observations of small-scale structures in Saturn’s dayside ultraviolet  
655 auroras - implications for physical origins, *J. Geophys. Res. (Submitted)*.

656 Meredith, C. J., I. I. Alexeev, S. V. Badman, E. S. Belenkaya, S. W. H. Cowley, M. K.  
657 Dougherty, V. V. Kalegaev, G. R. Lewis, and J. D. Nichols (2014), Saturn’s dayside  
658 ultraviolet auroras: Evidence for morphological dependence on the direction of the up-  
659 stream interplanetary magnetic field, *J. Geophys. Res. (Space Physics)*, *119*, 1994–2008,  
660 doi:10.1002/2013JA019598.

661 Miller, S., R. D. Joseph, and J. Tennyson (1990), Infrared emissions of H<sub>3</sub>(+) in the atmosphere  
662 of Jupiter in the 2.1 and 4.0 micron region, *Astrophys. J.*, *360*, L55–L58, doi:10.1086/185811.

663 Miller, S., T. Stallard, C. Smith, and et al. (2006), H<sub>3</sub><sup>+</sup>: the driver of giant planet atmospheres,  
664 *Phil. Trans. Roy. Soc. London.*, *364*, 3121–3137, doi:10.1098/rsta.2006.1877.

665 Miller, S., T. Stallard, H. Melin, and J. Tennyson (2010), H<sub>3</sub><sup>+</sup> cooling in planetary atmospheres,  
666 *Faraday Discussions*, *147*, 283, doi:10.1039/c004152c.

667 Moore, L., M. Galand, I. Mueller-Wodarg, R. Yelle, and M. Mendillo (2008), Plasma tem-  
668 peratures in Saturn’s ionosphere, *J. Geophys. Res. (Space Physics)*, *113*, A10306, doi:  
669 10.1029/2008JA013373.

670 Moore, L. E., M. Mendillo, I. C. F. Müller-Wodarg, and D. L. Murr (2004), Modeling of  
671 global variations and ring shadowing in Saturn’s ionosphere, *Icarus*, *172*, 503–520, doi:  
672 10.1016/j.icarus.2004.07.007.

673 Moses, J. I., and S. F. Bass (2000), The effects of external material on the chemistry and struc-

674 ture of Saturn’s ionosphere, *J. Geophys. Res.*, *105*, 7013–7052, doi:10.1029/1999JE001172.

675 Mueller-Wodarg, I. C. F., L. Moore, M. Galand, S. Miller, and M. Mendillo (2012),

676 Magnetosphere-atmosphere coupling at Saturn: 1 - Response of thermosphere and iono-

677 sphere to steady state polar forcing, *Icarus*, *221*, 481–494, doi:10.1016/j.icarus.2012.08.034.

678 Neale, L., S. Miller, and J. Tennyson (1996), Spectroscopic Properties of the  $H_3^+$  Molecule: A

679 New Calculated Line List, *The Astrophysical Journal*, *464*, 516, doi:10.1086/177341.

680 Nichols, J. D., S. V. Badman, E. J. Bunce, J. T. Clarke, S. W. H. Cowley, F. J. Crary, M. K.

681 Dougherty, J.-C. Gérard, D. Grodent, K. C. Hansen, W. S. Kurth, D. G. Mitchell, W. R.

682 Pryor, T. S. Stallard, D. L. Talboys, and S. Wannawichian (2009), Saturn’s equinoctial

683 auroras, *Geophysical Research Letters*, *36*, L24102, doi:10.1029/2009GL041491.

684 O’Donoghue, J., T. S. Stallard, H. Melin, G. H. Jones, S. W. H. Cowley, S. Miller, K. H.

685 Baines, and J. S. D. Blake (2013), The domination of Saturn’s low-latitude ionosphere by

686 ring ‘rain’, *Nature*, *496*, 193–195, doi:10.1038/nature12049.

687 O’Donoghue, J., T. S. Stallard, H. Melin, S. W. H. Cowley, S. V. Badman, L. Moore, S. Miller,

688 C. Tao, K. H. Baines, and J. S. D. Blake (2014), Conjugate observations of Saturn’s northern

689 and southern  $H_3^+$  aurorae, *Icarus*, *229*, 214–220, doi:10.1016/j.icarus.2013.11.009.

690 Oka, T. (2006), Interstellar Chemistry Special Feature: Interstellar  $H_3^+$ , *Proceedings of the*

691 *National Academy of Science*, *103*, 12,235–12,242, doi:10.1073/pnas.0601242103.

692 Provan, G., D. J. Andrews, C. S. Arridge, A. J. Coates, S. W. H. Cowley, S. E. Milan, M. K.

693 Dougherty, and D. M. Wright (2009), Polarization and phase of planetary-period magnetic

694 field oscillations on high-latitude field lines in Saturn’s magnetosphere, *J. Geophys. Res.*

695 *(Space Physics)*, *114*, A02225, doi:10.1029/2008JA013782.

696 Provan, G., D. J. Andrews, C. S. Arridge, A. J. Coates, S. W. H. Cowley, G. Cox, M. K.

697 Dougherty, and C. M. Jackman (2012), Dual periodicities in planetary-period magnetic

698 field oscillations in Saturn’s tail, *J. Geophys. Res. (Space Physics)*, *117*, A01209, doi:

699 10.1029/2011JA017104.

700 Provan, G., L. Lamy, S. W. H. Cowley, and M. K. Dougherty (2014), Planetary period os-



701 cillations in Saturn's magnetosphere: Comparison of magnetic oscillations and SKR mod-  
702 ulations in the post-equinox interval, *J. Geophys. Res. (Space Physics)*, submitted, doi:  
703 10.1002/2014JA020011.

704 Radioti, A., D. Grodent, J.-C. Gérard, S. E. Milan, B. Bonfond, J. Gustin, and W. Pryor  
705 (2011), Bifurcations of the main auroral ring at Saturn: ionospheric signatures of con-  
706 secutive reconnection events at the magnetopause, *J. Geophys. Res.*, *116*, A11209, doi:  
707 10.1029/2011JA016661.

708 Radioti, A., D. Grodent, J.-C. Gérard, B. Bonfond, J. Gustin, W. Pryor, J. M. Jasinski, and  
709 C. S. Arridge (2013), Auroral signatures of multiple magnetopause reconnection at Saturn,  
710 *Geophys. Res. Lett.*, *40*, 4498–4502, doi:10.1002/grl.50889.

711 Raynaud, E., E. Lellouch, J.-P. Maillard, G. R. Gladstone, J. H. Waite, B. Bézard, P. Drossart,  
712 and T. Fouchet (2004), Spectro-imaging observations of Jupiter's 2- $\mu$ m auroral emission. I.  
713 H<sub>3</sub><sup>+</sup> distribution and temperature, *Icarus*, *171*, 133–152, doi:10.1016/j.icarus.2004.04.020.

714 Sandel, B. R., and A. L. Broadfoot (1981), Morphology of Saturn's aurora, *Nature*, *292*, 679–  
715 682, doi:10.1038/292679a0.

716 Sandel, B. R., D. E. Shemansky, A. L. Broadfoot, J. B. Holberg, G. R. Smith, J. C. McConnell,  
717 D. F. Strobel, S. K. Atreya, T. M. Donahue, H. W. Moos, D. M. Hunten, R. B. Pomphrey,  
718 and S. Linick (1982), Extreme ultraviolet observations from the Voyager 2 encounter with  
719 Saturn, *Science*, *215*, 548–553, doi:10.1126/science.215.4532.548.

720 Smith, C. G. A., A. D. Aylward, G. H. Millward, S. Miller, and L. E. Moore (2007),  
721 An unexpected cooling effect in Saturn's upper atmosphere, *Nature*, *445*, 399–401, doi:  
722 10.1038/nature05518.

723 Southwood, D. (2011), Direct evidence of differences in magnetic rotation rate between Saturn's  
724 northern and southern polar regions, *J. Geophys. Res. (Space Physics)*, *116*, A01201, doi:  
725 10.1029/2010JA016070.

726 Southwood, D. J., and S. W. H. Cowley (2014), The origin of Saturn's magnetic periodicities:  
727 Northern and southern current systems, *J. Geophys. Res. (Space Physics)*, *119*, 1563–1571,

728 doi:10.1002/2013JA019632.

729 Stallard, T. S., H. Melin, S. Miller, J. O' Donoghue, S. W. H. Cowley, S. Badman, A. Adriani,  
730 R. H. Brown, and K. H. Baines (2012a), Temperature changes and energy inputs in giant  
731 planet atmospheres: what we are learning from  $\text{H}_3^+$ , *Phil. Trans. Roy. Soc.*, *370*, 5213–5224,  
732 doi:10.1098/rsta.2012.0028.

733 Stallard, T. S., H. Melin, S. Miller, S. V. Badman, R. H. Brown, and K. H. Baines (2012b),  
734 Peak emission altitude of Saturn's  $\text{H}_3^+$  aurora, *Geophys. Res. Lett.*, *39*, L15103, doi:  
735 10.1029/2012GL052806.

736 Yelle, R. V., and S. Miller (2004), *Jupiter's thermosphere and ionosphere*, pp. 185–218.